FE-Analysis of the Demagnetization Effect and Stress Inhomogeneities in MSMA Samples

Krishnendu Haldar, Bjoern Kiefer, Dimitris Lagoudas

FE-Analysis of the Demagnetization Effect and Stress Inhomogeneities in MSMA Samples

Journal:	*Philosophical Magazine & Philosophical Magazine Letters*
Manuscript ID:	TPHM-11-Jan-0038.R1
Journal Selection:	Philosophical Magazine
Date Submitted by the Author:	16-Jun-2011
Complete List of Authors:	Haldar, Krishnendu; Texas A&M University, Aerospace Engineering Kiefer, Bjoern; Institute of Mechanics, Department of Mechanical Engineering Lagoudas, Dimitris; Texas A&M University
Keywords:	magnetic alloys, shape memory alloys, FEM
Keywords (user supplied):	magnetic shape memory alloys (MSMA), demagnetization effect, magneto-mechanical coupling

Philosophical Magazine
Vol. 00, No. 00, Month 20xx, 1–24

RESEARCH ARTICLE

FE-Analysis of the Demagnetization Effect and Stress Inhomogeneities in MSMA Samples

Krishnendu Haldar[a], Björn Kiefer[b] and Dimitris C. Lagoudas[a]

[a]*Department of Aerospace Engineering, Texas A&M University College Station, TX 77843-3141, USA*;
[b]*Institute of Mechanics, TU Dortmund Leonhard-Euler-Str. 5, 44227 Dortmund, Germany.*

(*Received 00 Month 20xx; final version received 00 Month 20xx*)

Key Words: *magnetic shape memory alloys (MSMA), magnetostatics, demagnetization effect, magneto-mechanical coupling, coupled finite element analysis.*

ABSTRACT

This paper is concerned with the finite element analysis of boundary value problems involving nonlinear magnetic shape memory behavior, as might be encountered in experimental testing or engineering applications of MSMAs. The presented investigations mainly focus on two aspects: First, nonlinear magnetostatic analysis, in which the nonlinear magnetic properties of the MSMA are predicted by the phenomenological internal variable model previously developed by Kiefer and Lagoudas [1], is utilized to investigate the influence of the demagnetization effect on the interpretation of experimental measurements. An iterative procedure is proposed to deduce the true constitutive behavior of MSMAs from experimental data that typically reflect a sample shape-dependent system response. Secondly, the common assumption of homogeneous Cauchy stress distribution in the MSMA sample is tested. This is motivated by the expectation that the influence of magnetic body forces and body couples caused by field matter interactions may not be negligible in MSMAs that exhibit blocking stresses of well below 10 MPa. To this end, inhomogeneous Maxwell stress distributions are first computed in a post-processing step, based on the magnetic field and magnetization distributions obtained in the magnetostatic analysis. Since the computed Maxwell stress fields, though allowing a first estimation of the magnetic force and couple influence, do not satisfy equilibrium conditions, a finite element analysis of the coupled field equations is performed in a second step to complete the study. It is found that highly non-uniform Cauchy stress distributions result under the influence of magnetic body forces and couples, with magnitudes of the stress components comparable to externally applied bias stress levels.

*Corresponding author. Email: lagoudas@aero.tamu.edu

ISSN: 0950-0839 print/ISSN 1362-3036 online

DOI: 10.1080/09500839.20xx.xxxxxx
http://www.informaworld.com

1. Introduction

Magnetic shape memory alloys have recently drawn considerable research interest due to their ability to produce magnetic field-induced strains (MFIS) at least one order of magnitude higher than those of ordinary magnetostrictive materials [2–9]. The macroscopically observable *field-induced strains* in MSMA are caused by the microstructural *reorientation of martensitic variants*. Since the variants have different preferred directions of magnetization, applied magnetic fields can be used to select certain variants over others, which results in the macroscopic shape change.

This unique coupling of mechanical and magnetic properties makes MSMAs interesting materials for smart structures, actuator and sensor applications [10–13]. The most widely investigated magnetic shape memory materials are Ni-Mn-Ga alloys [14–17]. Martensitic transformations in Ni_2MnGa alloys were first conclusively reported by Webster et al. [18]. Zasimchuk et al. [19] and Martynov and Kokorin [20] performed detailed studies on the crystal structure of martensite in the Ni_2MnGa alloy. Ullakko et al. [21] are credited with first suggesting the possibility of a magnetic field-controlled shape memory effect in these materials. Other magnetic shape memory alloys that have been studied include Fe-Pd [2, 8, 22, 23], Fe-Ni-Co-Ti, Fe-Pt, Co-Ni-Ga, Ni-Mn-Al [24–29] and Co-Ni-Al [30, 31].

Several models have been proposed in the literature that describe the constitutive response related to the magnetic field-induced variant reorientation. For a detailed overview of the reported MSMA modeling work the reader is referred to [1, 32] and the review article by Kiang and Tong [33] as well as the references therein.

The model presented by James and Wuttig [23] is based on a *constrained theory of micromagnetics* (see also [34–36]). The terms contributing to the free energy in their model are the Zeeman energy, the magnetostatic energy and the elastic energy. O'Handley [4, 37] proposed a 2-D model in which two variants are separated by a single twin boundary and each variant itself consists of a single magnetic domain. Likhachev and Ullakko [38] presented a model which identifies the magnetic anisotropy energy difference in the two variant twinned-martensite microstructure as the main driving force for the reorientation process. Hirsinger and Lexcellent [39, 40] introduced the outline of a non-equilibrium thermodynamics-based model. Their free energy contains chemical, mechanical, magnetic and thermal contributions.

Kiefer and Lagoudas formulated a continuum thermodynamics-based phenomenological constitutive model for MSMAs with internal state variables describing the evolution of the crystallographic and magnetic microstructures. Their approach is aimed at capturing the hysteretic effects associated with the magnetic field-induced reorientation of martensitic twins and the resulting loading history dependence of the material response. Emphasis is also placed on modeling the nonlinear and stress-level-dependent nature of the magnetic field-induced strain and magnetization response. The Kiefer and Lagoudas model mainly distinguishes itself from the Hirsinger and Lexcellent approach by allowing the magnetization vectors to rotate away from the magnetic easy axes, which leads to much more accurate predictions of the magnetization response. Details of the model development were reported in [1, 32, 41–43]. Experimental characterization of MSMA response and the model validation were presented in [44]. The focus of this particular paper was placed on estimating the maximum MSMA actuator work output, both theoretically and experimentally. Furthermore, the numerical analysis of nonlinear magnetostatic boundary value problems for MSMAs was described in [45, 46]. More recently, stability analysis of magnetostatic boundary value problems for MSMAs was presented in [47].

Faidley et al. [48] proposed an extension of an earlier version of the Kiefer and Lagoudas model [41] to predict the reversible strain effect in Ni-Mn-Ga with collinear field and stress. In their approach internal restoring forces orthogonal to the applied field are attributed to pinning sites which elastically deform twin boundaries. Tan and Elahinia [49] utilized the Kiefer and Lagoudas model to study the dynamic response of MSMA actuators.

Despite these efforts, in the constitutive modeling of nonlinear, dissipative magnetic shape memory behavior two major complications have not yet been properly addressed in the literature and their significance remains unclear. The first is *the influence of non-ellipsoidal specimen geometries on measured and simulated magnetization curves*, the second is the *influence of magnetic body forces and body couples on the stress distribution* within a sample. Both of these issues are the subject of the work presented in this paper.

The well-known dependence of measured magnetization curves on specimen geometries is caused by the so-called *demagnetization effect*. From a modeling standpoint this effect complicates parameter identification as well as model validation, since the experimental data represent a sample geometry-dependent system response, not the true constitutive response. Typically, the correction of the data is carried out by making use of demagnetization factors that have been tabularized for ellipsoids of different aspect ratios. It is clear, however, that this technique loses its justification for non-uniform magnetization distributions as they typically occur in non-ellipsoidal specimen ([8]). This paper proposes an iterative procedure to properly interpret experimental data. The methodology is based on finite element solutions of nonlinear magnetostatic boundary value problems for MSMAs, which provide the necessary shape-dependent relations between applied and internal magnetic fields.

Furthermore, the validity of the common assumption of a spatially-uniform Cauchy stress within MSMA samples is tested. More precisely, the influence of magnetic body forces, magnetic body couples and thus Maxwell stress is typically assumed to be negligible. There exists theoretical and experimental evidence, however, that magnetic body forces may have an influence on both twin boundary motion, see discussion in O'Handley et al. [50], as well as stress-induced martensitic transformation, in Liang et al. [51]. In a first step of the present study, the Maxwell stress distributions resulting from spatially-varying magnetic body forces and magnetic body couples are computed in a post-processing manner based on the solution of the magnetostatic problem. It is found that the resulting Maxwell stress distributions are highly non-uniform. Encouraged by this observation, a coupled magneto-mechanical finite element analysis is performed to investigate the influence of Maxwell stress fields on Cauchy stress fields at equilibrium. It should be pointed out, that strictly speaking, this analysis is only partially coupled, since the influence of the feed-back of the stress variations to the nonlinear magnetic properties is neglected. Under this assumption, however, the results show strongly inhomogeneous distributions of the Cauchy stress with magnitudes of its components comparable to externally applied bias stress levels.

The structure of the paper is as follows: In Section 2 a brief summary of the magnetostatic problem and the phenomenological internal variable model for MSMAs developed by Kiefer & Lagoudas is given. Section 3 is concerned with the finite element analysis of a specific boundary value problem that is motivated by typical experimental set-ups. The nonlinear magnetic properties of the MSMA, used as input to the analysis, are provided by the constitutive model. In Section 4 the influence of the demagnetization effect on the interpretation of experimental data is analyzed in detail. In Section 5, Maxwell stress distributions are computed based on the

results of the magnetostatic analysis. By means of a coupled magneto-mechanical finite element analysis, non-uniform equilibrium Cauchy stress distributions are computed in Section 6, which properly account for the spatial non-uniformity of the Maxwell stress tensor. To conclude the paper, the significance of these findings for the modeling of MSMA behavior is discussed.

2. A Concise Review of the Magnetostatic Problem and the MSMA Constitutive Model

In the following section basic concepts of magnetostatics in the presence of magnetized matter are summarized to provide the foundation for the analysis of magnetostatic boundary value problems (BVPs) for MSMA materials. For static conditions in stationary bodies and negligible current density, Maxwell's equations in $\mathbb{R}^3$ are reduced to [52, 53]

$$\nabla\cdot\mathbf{B} = 0\,, \quad \text{and} \quad \nabla\times\mathbf{H} = \mathbf{0}\,, \tag{1}$$

where $\mathbf{B}$ is the magnetic induction and $\mathbf{H}$ is the magnetic field strength. These two quantities are related through the constitutive relation $\mathbf{B} = \mu_0(\mathbf{H}+\mathbf{M})$, in which μ_0 is the permeability of free space and $\mathbf{M}$ is the magnetization of a material point in a magnetized body, in this case a magnetic shape memory alloy sample. Equations (1) are subject to the jump conditions

$$[\![\mathbf{B}]\!]\cdot\mathbf{n} = 0\,, \quad [\![\mathbf{H}]\!]\times\mathbf{n} = \mathbf{0}\,, \tag{2}$$

on all interfaces, if surface currents are negligible. In Equations (2), $\mathbf{n}$ denotes the unit normal to the surface of discontinuity.

Taking advantage of the specific form of Equations (1), the magnetostatic problem is often reformulated, by deriving the magnetic field strength from a scalar potential Φ^m or the magnetic induction from a vector potential $\mathbf{\Phi}^m$. In the latter case $\mathbf{B} = \nabla\times\mathbf{\Phi}^m$ identically satisfies Equation (1a). Using the identity $\nabla\times(\nabla\times\mathbf{\Phi}^m) = \nabla(\nabla\cdot\mathbf{\Phi}^m) - \Delta\mathbf{\Phi}^m$, and the Coulomb gauge $\nabla\cdot\mathbf{\Phi}^m = 0$, Equation (1b) takes the form

$$\nabla\times(\mu_0^{-1}\nabla\times\mathbf{\Phi}^m - \mathbf{M}) = \mathbf{0}\,, \quad \text{or} \quad \Delta\mathbf{\Phi}^m = -\mu_0\nabla\times\mathbf{M}\,, \tag{3}$$

which is the *vector-valued Poisson equation* for the magnetic potential $\mathbf{\Phi}^m$.

For MSMAs the magnetization in Equation (3) is a function of the magnetic field and the loading history through a set of internal state variables $\boldsymbol{\zeta}$. The relation $\mathbf{M} = \mathbf{M}(\mathbf{H},\boldsymbol{\zeta})$ is provided by the constitutive model to be introduced shortly. Here we assume that the stress inside the material is uniform and remains constant at each material point before, during and after the reorientation process. At this point, the magnitudes of the body forces and body couples are assumed to be small and their contributions in the conservation of linear and angular momentum are neglected. The validity of this assumption is tested in Sections 5 and 6.

The MSMA constitutive relations to be used in the magnetostatic and later the magneto-mechanical analysis are provided by the Kiefer and Lagoudas phenomenological internal variable model [32, 42, 43]. This formulation is based on the Gibbs free energy function G, in which the Cauchy stress tensor $\boldsymbol{\sigma}$ and the magnetic field strength $\boldsymbol{H}$ are the independent state variables. The loading history dependence of the constitutive behavior, caused by dissipation associated with variant

rearrangement, is introduced through the evolution of internal state variables. The chosen internal state variables are the variant volume fraction ξ, the magnetic domain volume fraction α and the magnetization rotation angles $\theta_i (i{=}1{,}4)$. These variables are motivated by experimentally observed changes [54] in the crystallographic and magnetic microstructure. An idealized microstructural representation of twin martensitic phase is given in Figure 1. Two martensitic variants, variant-1 with volume fraction, ξ, and variant-2 with volume fraction, $1-\xi$, form 90^o magnetic domain walls and each variant contains 180^o domain walls. The volume fractions of 180^o magnetic domain wall in variant-1 and variant-2 are represented in Figure 1 by domain-1 and domain-2 and denoted by α and $1-\alpha$ respectively. The modeling approach is not limited to 2-variant microstructures. In the multi-variant case additional constraints must be enforced, e.g. sum over $\xi_i{=}1$. For the considered modeling problems, however, this addtitional complexity is not needed.

Figure 1. Schematic representation of the microstructure showing the coexistence of martensitic variants and magnetic domains.

The specific form of the Gibbs free energy for the Kiefer and Lagoudas model, having a typical two-dimensional setting in mind, is given by

$$G(\boldsymbol{\sigma}, \boldsymbol{H}, \xi, \alpha, \theta_i, \boldsymbol{\varepsilon}^r) = -\frac{1}{2\rho}\boldsymbol{\sigma} : \mathcal{S}(\xi)\boldsymbol{\sigma} - \frac{1}{\rho}\boldsymbol{\sigma} : \boldsymbol{\varepsilon}^r - \frac{\mu_0}{\rho}\boldsymbol{M}(\xi, \alpha, \theta_i) \cdot \boldsymbol{H} + \frac{1}{\rho} f(\xi, \alpha) + G^{an}(\xi, \alpha, \theta) + G_0(T_0) \ , \tag{4}$$

where ρ, $\mathcal{S}(\xi)$ are the density and the effective compliance tensor. The free energy function (4) is comprised of the elastic strain energy, the Zeeman energy, a mixing term (f), the magnetocrystalline anisotropy energy (G^{an}), and a reference state value (G_0). The Zeeman aims to align the magnetization with the magnetic field acting at a material point. The magnetocrystalline anisotropy energy can be viewed as the energy stored in the material due to the work done by an applied field in rotating the magnetization away from the magnetic easy axes. The mixing term accounts for the interaction of variants during the reorientation process.

The internal state variables ξ, α and θ_i can in general be connected with energy dissipation. In this phenomenological modeling approach they also account for loading history dependence of the constitutive response as caused by the thermodynamically irreversible evolution of the microstructure in a homogenized sense. Experimental results [14] show that the hysteresis for the single variant MSMA crystal specimen with respect to the magnetic easy axis and hard axis are almost negligible. This observation was expected for the case of the hard axis magnetization response, since the dominant mechanism, related with the magnetization rotation θ_i, is a reversible process. With regard to the easy axis magnetization, magnetic domain wall motion is the most important mechanism that can be associated with dissipation. In MSMA, however, the magnetic domain wall motion appears to be associated with a very small amount of dissipation. The dissipation in MSMAs is mainly due to variant reorientation mechanism which is caused due to the change in ξ, allowing to neglect the α dependency of the hardening function f. The internal variable $\boldsymbol{\varepsilon}^r$ is the generation of reorientation strain due to the evolution of ξ.

From the free energy expression (4) the magnetization constitutive equation is

derived in a thermodynamically-consistent manner as

$$\mathbf{M} = -\frac{\rho}{\mu_0}\frac{\partial G}{\partial \mathbf{H}} \ . \tag{5}$$

In the following analysis we consider two-dimensional boundary value problems that resemble typical experimental testing scenarios, see e.g. [44]. In these experiments, the MSMA sample is subjected to a constant compressive mechanical load along the x-axis and to a magnetic field along the perpendicular y-axis. The orientation of the single crystal specimen is [100] and is aligned with the direction of the mechanical load. The model through the evolution of α and ξ in general can capture both evolutions of 180 and 90 degree domain walls. The evolution of magnetic domains, although accounted for in the general framework, is neglected in this paper, since it only plays a significant role at low field and stress levels, see e.g. [43, 50]. To obtain more accurate predictions of the magnetization behavior it is, however, assumed that the MSMA sample is initially unmagnetized, which corresponds to a domain volume fraction value of $\alpha = 0.5$. This means equal volume fraction of the magnetic domains, separated by 180^o domain walls. Upon initiation of the forward reorientation process, i.e. from the stress-favored to the magnetic field-favored variant, it is assumed that all unfavored domains are instantaneously eliminated and α takes the value of 1. Under these assumptions the reduced form of the constitutive equations for the magnetization is given by [47]

$$\mathbf{M} = \begin{cases} \frac{\mu_0 M^{sat}}{2\rho K_1} H_y \mathbf{e}_y \ , & \text{for } \ \xi = 0 \ , \\ (1-\xi) M^{sat} \sqrt{1 - (\frac{\mu_0 M^{sat}}{2\rho K_1} H_y)^2}\ \mathbf{e}_x & \\ + \Big[(1-\xi) \frac{\mu_0 M^{sat}}{2\rho K_1} H_y + M^{sat} \xi \Big] \mathbf{e}_y \ , & \text{for } \ \xi \in (0,1) \\ M^{sat}\, \mathbf{e}_y & \text{for } \ \xi = 1 \ . \end{cases} \tag{6}$$

Here, $\mathbf{e}_x$ and $\mathbf{e}_y$ are the unit vectors along the x and y direction respectively. A closed-form expression for the evolution of the variant volume fraction during the forward reorientation process can be derived as [43]

$$\xi = \frac{1}{2}\cos\left[F_1 \left(\frac{(\mu_0 M^{sat})^2}{2\rho K_1} H_y^2 - \mu_0 M^{sat} H_y \right) + F_2 + \pi \right] + \frac{1}{2} \ . \tag{7}$$

Specific relations between the constants F_1 and F_2 and the model parameters M^{sat}, ρK_1, $H_y^{s(1,2)}$, $H_y^{f(1,2)}$, σ^* and $\varepsilon^{r,max}$, namely the saturation magnetization, the magnetocrystalline anisotropy constant, the critical field values for the start and finish of the forward reorientation process, the blocking stress and the maximum reorientation strain are given in [43]. The model parameters must be identified from experiments. The specific calibration used in the following simulations is based on experimental data reported in [44]. The resulting parameter values are listed in Table 1.

Figure 2. The x and y-components of the predicted magnetization response.

Table 1. Material parameters calibrated for the $Ni_{51.1}Mn_{24.0}Ga_{24.9}$ composition tested at a compressive stress level of -2 MPa [44].

Material Parameters					
Quantity	Value	Unit	Quantity	Value	Unit
ρK_1	700.0	kJm^{-3}	$\mu_0 H_y^{s(1,2)}$	0.9	T
M^{sat}	742.4	kAm^{-1}	$\mu_0 H_y^{f(1,2)}$	1.85	T
$\varepsilon^{r,max}$	5.65	%	$\mu_0 H_y^{s(2,1)}$	0.75	T
σ^*	-2.0	MPa	$\mu_0 H_y^{f(2,1)}$	-0.17	T

The predicted magnetization response curves are plotted in Fig. 2 and may be explained in the following way. Initially, the sample consists of the stress-favored variant and two oppositely magnetized domains of equal volume fraction separated by 180° domain walls, such that it is macroscopically unmagnetized. When magnetic field is applied along the y-direction, the hard axis of the stress-favored variant, the magnetization vectors start to rotate in each domain. The x-components of the magnetization vectors in the adjacent domains cancel each other, while their y-components add up. Once the critical field for the variant reorientation has been reached, the field-favored variant nucleates and magnetization curve becomes nonlinear. As pointed out above, it is assumed that unfavorable magnetic domains are eliminated simultaneously with the activation of the reorientation process due to comparatively high magnetic field (see also [55, 56]). This results in a sharp increase of the M_x-component of the predicted magnetization curve. After the reorientation process is completed, only the single-domain, field-favored variant remains and the magnetic saturation level is reached with the magnetization vector fully-aligned along the applied field direction, which coincides with the easy axis of the field-favored variant.

3. Finite Element Analysis of the Nonlinear Magnetostatic Problem

Based on the field equations and the MSMA constitutive relations derived in the previous section we can now proceed with the solution of specific nonlinear magnetostatic boundary value problems using the finite element method. The numerical analysis presented in this paper was performed using the COMSOL Multiphysics finite element software package.

The geometry and boundary conditions of the considered model problem are illustrated in Figure 3. This particular arrangement is motivated by the experimental set up reported in [44]. The computational domain may be regarded as the gap between the pole pieces of an electromagnet of dimensions $26\,\text{mm} \times 26\,\text{mm} \times 26\,\text{mm}$ for which a uniform magnetic field of up to 2 T can be applied. Typical specimen dimensions are $8\,\text{mm} \times 4\,\text{mm} \times 4\,\text{mm}$, or aspect ratios of $2:1:1$, where the long axis is the x-direction.

A spatially constant magnetic potential

$$\Phi_x^m = \Phi_y^m = 0\,; \quad \Phi_z^m = -\mu_0 H_y^a x\,, \tag{8}$$

is applied on all sides of the boundary, such that with Equation (3) it follows

$$\mu_0 H_x = B_x = \frac{\partial \Phi_z^m}{\partial y} - \frac{\partial \Phi_y^m}{\partial z} = 0 \ , \quad \mu_0 H_y = B_y = \frac{\partial \Phi_x^m}{\partial z} - \frac{\partial \Phi_z^m}{\partial x} = \mu_0 H_y^a \ ,$$

$$\mu_0 H_z = B_z = \frac{\partial \Phi_y^m}{\partial x} - \frac{\partial \Phi_x^m}{\partial y} = 0 \ , \tag{9}$$

i.e. the desired homogeneous magnetic field in the computational domain in the absence of the specimen. The presence of the magnetizable sample, of course, perturbs the homogeneity of the applied field.

Figure 3. Domain geometry, mesh and boundary conditions for the magnetostatic problem.

The following comments must be made regarding the usage of the magnetization data in the magnetostatic analysis:

(1) The stress is assumed to be uniaxial, at a constant level and spatially homogeneous, since magnetic body forces and magnetic body couples are neglected. The only coupling between the mechanical and the magnetostatic problem at this point is given by the stress level dependence of the magnetic properties. Thus for each stress level the magnetostatic analysis has to be performed in a separate computation.

(2) The magnetic field, and thus the magnetization, on the other hand vary spatially inside the rectangular specimen. The magnetic properties predicted by the constitutive model are evaluated at every integration point in the finite element mesh. Since the magnetization nonlinearly depends on the magnetic field, the magnetostatic problem is highly nonlinear. COMSOL Multiphysics provides an appropriate iterative nonlinear solver. The parametric version of this solver was used such that the magnetic field distribution could be computed, while scaling the applied magnetic field from 0 T to 2 T.

(3) Although a magnetic potential difference was applied to represent a homogeneous external field whose x-component is zero, see Equation (9), the magnetic field in the MSMA specimen is non-uniform and exhibits a non-zero x-component, particularly at the corners of the sample. The constitutive dependency $\mathbf{M}(H_x)$ is assumed to be small and thus neglected, see Equations (6).

(4) The hysteretic nature of the constitutive response is not addressed in the magnetostatic analysis at this point. To be precise, the hysteresis is not neglected, but the analysis is only carried out for monotonous loading from 0 T to 2 T, not for the removal of the magnetic field.

Numerical results of the finite element analysis are plotted in Figure 4 in terms of the distribution of the y-component of the magnetic field for the exemplary applied magnetic induction level of 2 T.

Figure 4. Distribution of H_y in the computational domain at the applied magnetic field of $\mu_0 H_y^a = 2.0$ T.

It is observed that indeed, due to the non-ellipsoidal shape of the specimen, the

magnetic field and thus the magnetization are non-uniform inside the specimen although a constant magnetic induction is applied at the boundary of the computational domain. The presence of the magnetized specimen clearly perturbs the magnetic field in the free space surrounding the sample. From this distribution one can for example obtain information to which extent a Hall probe reading, used to measure the applied field, can be expected to be influenced by the sample's magnetic field. The distribution at 2.0 T, at which essentially all of the material has been magnetized to saturation along the y-axis, is symmetric with respect to both axes of the coordinate system.

It again must be emphasized that in the magnetostatic problem the magnetization is allowed to change locally and its value is determined by evaluating the magnetization curve for the magnetic field acting at the particular point. The internal mechanism which leads to the macroscopic magnetization response, namely the evolution of the martensitic variants, the magnetic domains and the magnetization rotation angles as predicted by the constitutive model have been discussed earlier. Such a modeling approach assumes that there exists a separation of scales such that at each point in the continuum, the MSMA sample, there exist a smaller length scale at which a sufficient number of martensitic twins and magnetic domains coexist such that average quantities like the magnetization can be defined for each point. The contributions of the variant and magnetic domains are then taken into account phenomenologically in a homogenized sense and are no longer "visible" on the continuum scale. It is still a matter of discussion whether this approach is fully justified for MSMA single crystals.

Figure 5. (a) Distribution of the magnetic field and (b) magnetization within the specimen at the applied magnetic field of $\mu_0 H_y^{\mathrm{a}} = 1.3$ T.

To take a closer look at the local solution, the variation of the computed magnetic field within the MSMA sample is plotted in Figure 5 for a specific applied field level. In Figure 6 the variation of the magnetic field and the magnetization across the specimen are plotted for different locations. Note that at the left ($y = -2$) and right ($y = 2$) sides of the specimen the jump in the magnetic field balances the jump of the magnetization in the transition from free space into the magnetized material. The magnetic induction component $B_y = \mu_0(H_y + M_y)$, which is the normal component of the magnetic induction on these interfaces, thus stays constant, so that the jump condition specified in Equation (2a) is properly satisfied.

Figure 6. (a) Distribution of the y-components of the magnetic field and (b) the magnetization across the specimen and its immediate vicinity at different levels of x, as indicated in Figure 5, at the applied magnetic induction level of 1.3 T.

4. Influence of the Demagnetization Effect on the Interpretation of Experiments

From the theory of magnetostatics it is well-known, that the magnetic field caused by the magnetization of the material opposes the direction of magnetization. It is therefore called the *demagnetizing or self field*. This *demagnetization effect* can also clearly be observed in the plots of Figure 6. Furthermore, as a consequence of the interface conditions of Equations (2), the demagnetization field in a uniformly

magnetized ellipsoidal sample is always uniform, while it is non-uniform in a non-ellipsoidal sample. Permanent magnets, by definition, exhibit substantial remnant macroscopic magnetization at zero applied field and, within certain limits, the magnetization of the magnetic sample does not depend on the applied magnetic field [57]. For magnetostatic problems involving only permanent magnets the Poisson equation (3) is linear and the principle of superposition holds. Thus, if additionally an external magnetic field $\mathbf{H}^a$ is applied, the total magnetic field is then given by

$$\mathbf{H} = \mathbf{H}^a + \mathbf{H}^d \,. \tag{10}$$

General integral representations of the solution of the magnetostatic problem defined by Equation (3) exist, see e.g. [52, 58]. For uniformly magnetized bodies the magnetization vector can be taken outside the integral expressions for the magnetic field strength [58, 59], such that

$$\mathbf{H}^d(\mathbf{r}) = -\underbrace{\left[\frac{1}{4\pi}\iint\limits_{\partial\Omega^m} \frac{\mathbf{r}-\mathbf{r}'}{|\mathbf{r}-\mathbf{r}'|^3} \otimes \mathbf{n}' \,\mathrm{d}A'\right]}_{=:\mathbf{D}} \mathbf{M} = -\mathbf{D}\mathbf{M} \,. \tag{11}$$

Therein $\mathbf{r}$ is the position at which $\mathbf{H}$ is evaluated in $\mathbb{R}^3$ and $\mathbf{r}'$ the location of a point on the surface $\partial\Omega^m$, with unit outward normal $\mathbf{n}'$, of the region Ω^m occupied by the magnetized body. By applying the divergence theorem, an equivalent volume integral representation of Equation (11) can be obtained. $\mathbf{D}$ is the *demagnetization tensor*, which only depends on the geometry of the body and can be computed by evaluating the bracketed integral expression in Equation (11). For a spatially uniformly magnetized body the demagnetization field can thus be computed by simply multiplying the magnetization with an appropriate demagnetization factor. Such factors have been tabularized for ellipsoids of many different aspect ratios [57, 60, 61]. This procedure is analogous to using Eshelby tensors in elasticity theory to determine the strain field inside ellipsoidal inclusions [62, 63]. The demagnetization tensor has the following properties: i) it is independent of position inside an ellipsoidal body; ii) it is diagonal if its eigenvectors are aligned with the symmetry axes of the body; iii) its trace is 1, if evaluated inside the body. The demagnetization factor for a sphere is therefore 1/3 in any direction. For a prismatic cylinder with square or circular cross-section the axial and transverse demagnetization factors are related by $D^t = 1/2(1 - D^a)$, see [64].

The magnetic field inside a uniformly magnetized sample of non-ellipsoidal shape is always non-uniform. The demagnetization tensor in this case depends on the position inside the sample. It is customary to define average demagnetization tensors for samples of arbitrary shape, sometimes referred to as *magnetometric demagnetization tensors* [64, 65], in the following manner

$$\langle \mathbf{D} \rangle := \frac{1}{\Omega^m} \int\limits_{\Omega^m} \mathbf{D}(\mathbf{r}) \,\mathrm{d}V \,. \tag{12}$$

The average demagnetization field can then be written, for uniform magnetization $\mathbf{M}$ as

$$\langle \mathbf{H}^d \rangle = -\langle \mathbf{D} \rangle \mathbf{M} \,. \tag{13}$$

Numerical solution schemes have been developed to determine the demagnetiza-

tion factors for uniformly magnetized bodies of arbitrary shape. They have been computed and documented for many standard geometries, such as prismatic bars with different cross-sectional shapes [59, 64, 65].

By definition the demagnetization factor loses its meaning for bodies with non-uniform magnetization. Thus, the exact demagnetization field inside a non-ellipsoidal body, whose magnetization is induced by an external magnetic field and therefore not uniform unless complete saturation is reached at high fields, can not be computed with the help of demagnetization factors. In this case, which is always encountered in experiments unless ellipsoidal specimen are used, an explicit numerical solution of the magnetostatic boundary value problem has to be obtained. For MSMAs the problem is complicated by the fact that the magnetic properties are nonlinear, hysteretic and stress level dependent. Furthermore, the shape of the sample changes due to the magnetic field-induced strain. This effect, however, is expected to be small and is neglected within the small strain theory.

On the basis of the magnetostatic analysis presented above, it is now possible to derive an iterative procedure in which the computed load-dependent relation between the applied field and the internal field is utilized to reinterpret the experimental data by accounting for the demagnetization effect. This must be understood as the *inverse problem* of identifying the model parameters such that the simulation results in the applied magnetic field vs. magnetization curve are measured in the experiment for a specific sample geometry.

The first magnetostatic simulation is typically performed using the model parameters obtained from a parameter identification based on the *uncorrected* data. In these magnetostatic simulations, which, except for the assumption of a given constant stress level, are decoupled from the mechanical equations, the material properties are taken into account in terms of a nonlinear magnetization curve. Thus the relation between the internal and applied field computed in one run of the analysis can only serve to find a first correction of the experimental data. Thus the nonlinear magnetization data, which was originally known in terms of the constant applied field, is now known in terms of the average internal magnetic field with the accuracy of the first iteration. Then the model parameters are re-identified based on the corrected data and the analysis is repeated with the output of first iteration as next input. The simulation result can once again be used to correct the magnetization curve. By following this procedure, the relation between the applied field and the internal field is computed more accurately in each iteration step. For our example, the original and corrected magnetization curves resulting from this iterative procedure are depicted in Figure 7 for the considered specimen with 2:1 length to width ratio. For conciseness, only the correction of the average magnetization $\langle M_y \rangle$-component is presented here (Figure 7).

Figure 7. Magnetization data iteratively corrected for demagnetization. Specimen aspect ratio 2:1.

The corrected procedure may also be interpreted as keeping the same data for the magnetization axes, while rescaling the magnetic field axis by means of the relation between the average internal and applied field at each iteration. One observes the relatively fast convergence of the solution. After six iterations the difference to the solution of the previous iteration is small enough to conclude that the solution has converged. The magnetization curve of iteration six can thus be considered the "true" magnetization response, which is independent of the specimen geometry. The original data on the other hand is the magnetization behavior that would be measured in an experiment using a prismatic sample of this aspect ratio. In an

experiment that uses a sample of the same material, but different aspect ratio a different curve would be measured.

A parametric study has been performed to investigate the sample shape dependence of the demagnetization effect for the prismatic specimen with nonlinear magnetic properties. In Figure 8 the corrected magnetization data has been plotted for four different aspect ratios of the prismatic specimen. The corresponding corrections of the magnetic field-induced strain data have been plotted in Figure 9. It is clearly observed that the influence of the specimen aspect ratio on the difference between the apparent material behavior and the true constitutive response is very significant and must therefore be addressed when using data for model calibration. Once the MFIS data has been corrected for demagnetization, the model parameters can be calibrated correctly.[1]

Figure 8. Influence of specimen aspect ratios on the correction of the magnetization data.

Figure 9. Influence of specimen aspect ratios on the correction of the magnetic field-induced strain data.

One of the stated goals of this analysis is to compare the differences in the demagnetization correction by the demagnetization factor method and the finite element analysis. The first method is based on the relation

$$\langle H_y \rangle = H_y^a + \langle H_y^d \rangle = H_y^a - \langle D_{yy} \rangle M_y \ , \tag{14}$$

which follows from Equations (12), (10) and (13). This procedure of course assumes that the magnetization in the sample is uniform. Shield acknowledges in [8] that the demagnetization factor method can therefore only lead to approximations of the demagnetization effect in the prismatic samples typically used in MSMA testing. Nonetheless, this method is often used due to its simplicity or lack of alternatives. However, it is not clear beforehand what kind of error one might expect from making this approximation. With the developed simulation capabilities this error can now be quantified.

Since a literature value was not available for this particular geometry, the factor of $\langle D_{yy} \rangle = 0.65$ was computed using a two-dimensional magnetostatic finite element simulation for a permanent magnet sample, i.e. with spatially uniform and field-independent magnetization $M_y = \langle M_y \rangle$, of rectangular geometry with a 2:1 aspect ratio placed in a free space domain. This technique has proven to yield very accurate demagnetization factors for other geometries for which literature data was available [4, 64]. The different correction methods are compared in Figure 10.

Figure 10. Comparison of the corrections using the demagnetization factor method and nonlinear FE-analysis. Specimen aspect ratio 2:1.

These observations suggest that by using the demagnetization factor method, which is based on the assumption of uniform magnetization in the specimen, one obtains essentially the same result as performing the FE-analysis of the nonlinear magnetostatic problem with non-uniform magnetization, if average field variables

[1] The specific results presented here are based on solutions of 2-D boundary value problems and can thus only be used for a qualitative assessment. The procedure is the same for 3-D problems, which, however, are computationally much more involved.

are considered. This conclusion can be misleading, however, since it only holds for average quantities. But as evident from Figure 5 and Figure 6, there exists a significant variation in the local magnetization. To further quantify this variation, Figure 11 displays local values of the magnetic field at several points in the specimen as a function of the applied field. For problems in which the knowledge of the local magnetic field and magnetization is important, one can not avoid solving the magnetostatic problem explicitly. This is certainly the case for magneto-mechanical boundary value problems involving more complicated, technologically-relevant geometries, e.g. MSMA components in actuators applications.

Figure 11. Position dependence of the magnetization response within the rectangular specimen.

5. Post-Processing Computation of Maxwell Stress Distributions

The second major focus of this paper is to employ the FE-analysis in the investigation of possible stress inhomogeneities in the MSMA sample due to magnetic body forces and body couples. A first estimate of the influence of this effect can be obtained by computing the *Maxwell stress* distribution in a post-processing manner using the relation [66]

$$\boldsymbol{\sigma}^M = \mu_0 \mathbf{H} \otimes \mathbf{H} + \mu_0 \mathbf{H} \otimes \mathbf{M} - \frac{1}{2}\mu_0 (\mathbf{H}\cdot\mathbf{H})\mathbf{I} \,, \tag{15}$$

The Maxwell stress tensor, by definition, accounts for the magnetic body forces and couples in the following manner

$$\nabla \cdot \boldsymbol{\sigma}^M = \rho \mathbf{f}^m = \mu_0 (\nabla \mathbf{H})\mathbf{M} \,, \tag{16}$$

$$\operatorname{skw}(\boldsymbol{\sigma}^M) = -\rho \mathbf{L}^m = -\operatorname{skw}(\mu_0 \mathbf{M} \otimes \mathbf{H}) \,. \tag{17}$$

The body couple vector $\rho \mathbf{l}^m$ is the dual vector of $\rho \mathbf{L}^m$ such that $\mathbf{L}^m \mathbf{a} = \mathbf{l}^m \times \mathbf{a}$

Figure 12. The x and y-components of the corrected magnetization curves used in the Fe-analysis.

for any vector $\mathbf{a}$. We investigate the distributions of the magnetic body force, body couple and Maxwell stress based on the numerical solution of the magnetostatic problem at the exemplary applied magnetic induction value of $\mu_0 \langle H_y \rangle = 1\,\mathrm{T}$. We chose this load level because, as evident from Figure 12, it is close to the end of the reorientation region, where the intensity of the magnetic field is high.

(a) (b)

Figure 13. (a) Field-induced martensitic volume fraction and (b) normalized magnetization vector distribution at $\mu_0 \langle H_y \rangle = 1\,\mathrm{T}$.

A contour plot of the field-favored variant volume fraction ξ is depicted in Figure 13(a). The legend shows that ξ ranges from 0.93 to 1.0, such that at this load level the reorientation process is either finished or near completion at every point in the sample. Correspondingly, the normalized magnetization vectors of Figure 13(b) are aligned with the applied field direction.

(a) (b)

Figure 14. (a) σ^M_{xx} and (b) σ^M_{yy}-component distribution of the Maxwell stress (MPa) at $\mu_0\langle H_y\rangle = 1$ T.

The four planar components of the non-symmetric Maxwell stress at the considered load level are shown in Figs. 14 and 16. Highly non-uniform distributions of the Maxwell stress components are observed, which through Equation 15 are directly correlated with the spatially inhomogeneous magnetic field and magnetization field. Specific values of the Maxwell stress components are listed in Table 2 for the representative locations P_0 to P_8 indicated in Figure15.

Table 2. Maxwell stresses (MPa) at $\mu_0\langle H_y\rangle = 1$ T.

	P_0	P_1	P_2	P_3	P_4	P_5	P_6	P_7	P_8
σ^M_{xx}	-0.336	-0.444	-0.416	-0.329	-0.416	-0.444	-0.416	-0.329	-0.416
σ^M_{yy}	1.011	1.227	1.178	0.996	1.178	1.227	1.178	0.996	1.178
σ^M_{xy}	-0.036	0.004	-0.163	-0.032	0.173	0.005	-0.163	-0.032	0.173
σ^M_{yx}	0.000	0.003	-0.085	0.001	0.090	0.002	-0.085	0.001	0.090

Figure 15. Location of nine representative points at which the numerical solution is explored in detail. Here Ω represents material domain

Note that the σ^M_{xx} component is purely compressive in nature. Furthermore, magnitudes of nearly 21% of the applied traction of -2 MPa are observed. This implies that this component could potentially influence the formation of the stress-favored variant significantly. The σ^M_{yy}-component on the other hand is tensile, which, however, would enhance the tendency to hinder the forward reorientation process.

(a) (b)

Figure 16. (a) σ^M_{xy} and (b) σ^M_{yx}-component distribution of Maxwell stress (MPa) at $\mu_0\langle H_y\rangle = 1$ T.

(a) (b)

Figure 17. (a) Magnetic body couple at $\mu_0\langle H_y\rangle = 1$ T and (b) orientation of magnetization and magnetic field vectors.

According to Equation (17b), the σ^M_{xy} and σ^M_{yx} components displayed in Figure 16 are directly correlated with the magnetic body couple. The computed body couple component values are given in Table 3 for the selected points. If we consider point P_2, for example, the value of the magnetic moment is $0.039\,\mathrm{Nmm/mm^3}$ and it acts clockwise. The shear stress components at this point are $\sigma^M_{xy} = -0.163$ MPa and $\sigma^M_{yx} = -0.085\,\mathrm{MPa}$, see Table 2, and they contribute to balance the magnetic body couple.

Table 3. Out of plane body couple vector ($\mathrm{Nmm/mm^3}$) at $\mu_0\langle H_y\rangle = 1\,\mathrm{T}$. The positive sign means anti-clockwise and the negative negative sign means clockwise direction.

	P_0	P_1	P_2	P_3	P_4	P_5	P_6	P_7	P_8
ρL^m	0.018	-0.001	0.039	0.021	-0.041	-0.001	0.039	0.02	0.041

Figure 17(a) shows the non-uniform variation of the magnetic body couple at $\mu_0\langle H_y\rangle = 1\,\mathrm{T}$. The magnitude of the body couple is observed to have higher values near the corners of the sample as compared to its center. This may be explained by the fact that the body couple vector is computed from the cross product between the magnetic field and magnetization vectors, such that high values result close to the corners, where the magnetic field intensifies and larger relative angles between these vectors occur. This is also illustrated in Figure 17(b). Here, the two sets of arrows at each point represent magnetization vectors (light arrows) and magnetic field vectors (dark arrows), respectively. It should be noted, that the magnetic field vector changes orientation from the corner region C_1 to C_2, see Figure 17(a). Due to the point-symmetric nature of the numerical solution, an opposite trend of the sign change is observed between regions C_3 to C_4. The shear stress components show a similar trend in their spatial distributions.

The intensity of the body force on the other hand depends on the gradient of the magnetic field. Spatial distributions of the body force components are plotted in Figure 18 and corresponding numerical values for points P_0 to P_8 are given in Table 4. Since the gradient of magnetic field is high near the sample corners, the body force are large in these regions. Their magnitude decreases near the center of the specimen, where the magnetic field distribution is relatively uniform.

(a) (b)

Figure 18. (a) ρf^m_x and (b) ρf^m_y component distributions ($\mathrm{N/mm^3}$) at $\mu_0\langle H_y\rangle = 1\,\mathrm{T}$.

Table 4. Body force values ($\mathrm{N/mm^3}$) at $\mu_0\langle H_y\rangle = 1\,\mathrm{T}$.

	P_0	P_1	P_2	P_3	P_4	P_5	P_6	P_7	P_8
ρf^m_x	-0.001	-0.080	-0.077	0.005	0.078	0.080	0.077	-0.005	-0.080
ρf^m_y	0.000	0.000	-0.046	-0.012	-0.045	0.000	0.046	0.012	0.045

6. Finite Element Analysis of the Magneto-Mechanically-Coupled Field Equations for MSMA

The results in the previous section show that the intensity of the Maxwell stress components is significant compared to the applied tractions. This observation motivates us to solve a *coupled magneto-mechanical problem* to investigate the influence

of the magnetic body forces and body couples on the Cauchy stress in an equilibrium configuration. The magnetic boundary conditions are the same as described for the magnetostatic problem. The mechanical boundary conditions of the problem are illustrated in Figure 19, where t_x and t_y denote the mechanical traction on the boundaries along the x- and the y-directions, respectively. The compressive traction along the x-direction is imposed by constraining the vertical displacement U of the $\partial\Omega_3$ surface and by applying a mechanical load $P = 2$ MPa on the $\partial\Omega_1$ surface. We fixed the point R to eliminate rigid body motion in the finite element analysis.

Figure 19. Imposed mechanical boundary conditions. Ω is the material domain and $\partial\Omega$ its boundary.

In addition to the field equations of the magnetostatic problem described in Section 2, the magneto-mechanical problem is described by the conservation of linear momentum and the conservation of angular momentum for the magnetic continuum [66, 67]

$$\nabla\cdot\boldsymbol{\sigma} + \rho\mathbf{f} + \rho\mathbf{f}^m = \mathbf{0} \qquad \text{in } \Omega\,, \tag{18a}$$

$$\operatorname{skw}\boldsymbol{\sigma} = \rho\mathbf{L}^m \quad \text{in } \Omega\,. \tag{18b}$$

The expressions for the Maxwell stress tensor, the magnetic body force and the magnetic body couple were given in Equations (15), (16) and (17). By defining the *total stress tensor* as $\boldsymbol{\sigma}^t := \boldsymbol{\sigma} + \boldsymbol{\sigma}^M$, the mechanical equilibrium equations may also be re-written in the more convenient form

$$\nabla\cdot\boldsymbol{\sigma}^t + \rho\mathbf{f} = \mathbf{0}\,, \quad \text{and} \quad \operatorname{skw}\boldsymbol{\sigma}^t = \mathbf{0}\,, \quad \text{in } \Omega\,. \tag{19}$$

A detailed derivation of the *magneto-mechanical boundary conditions* is given in the appendix.

The presence of the magnetic body couple causes the Cauchy stress tensor to be non-symmetric. The Cauchy stress may be decomposed in the following manner, see e.g. [66, 67],

$$\boldsymbol{\sigma} = \boldsymbol{\sigma}^{MT} - \mu_0(\mathbf{H}\otimes\mathbf{M})\,, \tag{20}$$

where $\boldsymbol{\sigma}^{MT}$ is a symmetric tensor that can be interpreted as the *mechanical part* of the Cauchy stress tensor. We then modify the proposed Gibbs free energy function (4) by assuming a dependence on $\boldsymbol{\sigma}^{MT}$, rather then the non-symmetric Cauchy stress $\boldsymbol{\sigma}$. The modified expression is given by

$$\begin{aligned} G(\boldsymbol{\sigma}^{MT}, \boldsymbol{H}, \xi, \alpha, \theta_i, \boldsymbol{\varepsilon}^r) = &-\frac{1}{2\rho}\boldsymbol{\sigma}^{MT} : \mathcal{S}\boldsymbol{\sigma}^{MT} - \frac{1}{\rho}\boldsymbol{\sigma}^{MT} : \boldsymbol{\varepsilon}^r - \frac{\mu_0}{\rho}\boldsymbol{M}\cdot\boldsymbol{H} \\ &+ \frac{1}{\rho}f(\xi,\alpha) + G^{an}(\xi,\alpha,\theta) + G_0(T_0)\,. \end{aligned} \tag{21}$$

The constitutive equation for the total infinitesimal strain tensor then follows as

$$\boldsymbol{\varepsilon} = -\rho\frac{\partial G}{\partial\boldsymbol{\sigma}^{MT}} = \mathcal{S}\boldsymbol{\sigma}^{MT} + \boldsymbol{\varepsilon}^r\,, \tag{22}$$

or the inverse relation

$$\boldsymbol{\sigma}^{MT} = \mathbf{C} : \boldsymbol{\varepsilon}^{\mathbf{e}} = \mathbf{C} : (\boldsymbol{\varepsilon} - \boldsymbol{\varepsilon}^{\mathbf{r}}) \; . \tag{23}$$

The newly introduced variables are the elasticity tensor $\mathbf{C}$ and the reorientation tensor $\mathbf{\Lambda}$. The latter determines the direction in which the reorientation strain develops according to $\boldsymbol{\varepsilon}^r = \mathbf{\Lambda}\xi$ and its specific form for the considered two-dimensional problem is given in Table 5. It should be noted that the constitutive relation for the magnetization remains unchanged.

Using the decomposition of the Cauchy stress (20) in Equation (18a), the conservation of linear momentum for the magnetic continuum under static conditions and negligible non-magnetic body forces may be written as

$$\nabla \cdot (\boldsymbol{\sigma}^{MT} - \mu_0 \mathbf{H} \otimes \mathbf{M}) + \rho \mathbf{f}^m = \mathbf{0} \; . \tag{24}$$

This expression can be simplified as follows

$$\begin{aligned} \nabla \cdot \boldsymbol{\sigma}^{MT} + [\rho \mathbf{f}^m - \nabla \cdot (\mu_0 \mathbf{H} \otimes \mathbf{M})] = \mathbf{0} \; , \\ \nabla \cdot \boldsymbol{\sigma}^{MT} + [\mu_0 (\nabla \mathbf{H}) \mathbf{M} - (\mu_0 \mathbf{H} (\nabla \cdot \mathbf{M}) + \mu_0 (\nabla \mathbf{H}) \mathbf{M})] = \mathbf{0} \; , \\ \nabla \cdot \boldsymbol{\sigma}^{MT} + [-\mu_0 \mathbf{H} (\nabla \cdot \mathbf{M})] = \mathbf{0} \; . \end{aligned} \tag{25}$$

Table 5 summarizes the coupled problem consisting of the magneto-mechanical field equations, the constitutive relations and boundary conditions. In addition to the material parameters used in the nonlinear magnetostatic analysis, isotropic mechanical properties of the martensitic phase are assumed for simplicity, with a Young's modulus of 2.0 GPa and a Poisson's ratio of 0.3 (cf. [68], [17]).

It should be emphasized that the problem solved in the finite element analysis as defined in Table 5 is only *partially coupled*, since the stress dependence of the magnetic response, although captured in the general formulation of the constitutive model, has been neglected. This is usually valid since all tests are preformed at a constant stress level. In the considered case the coupling thus only exists through the presence of magnetic body forces and couples in the mechanical equilibrium equations. Numerical solutions of the coupled problem in terms of the distributions of the magnetic field variables are therefore *identical* to those of the uncoupled magnetostatic problem presented in the previous section. Nonetheless, this approach is expected to yield much more realistic solutions for the Maxwell stress distributions, because they now satisfy mechanical equilibrium. Furthermore, the spatial variation of the Cauchy stress field under the influence of magnetic body forces and body couples can now be computed, which was the main objective of the numerical analysis.

The computed Cauchy stress field components are shown in the iso-line plots of Figure 20 for the applied magnetic induction level of $\mu_0 \langle H_y \rangle = 1$ T. It is observed that the Cauchy stress distribution is, as expected, also strongly non-uniform in the specimen. Detailed numerical data of these components at the nine representative points P_0 to P_8 are given in the Table 6.

Note that the deviation of the axial Cauchy stress σ_{xx} from the typically assumed homogeneous stress of -2.0MPa is substantial. The local relative difference of these values is listed in Table 7. The results show that the change in magnitude can be up to 80 %. The maximum compressive stress value of -3.58 MPa occurs at the center of the specimen. The value of the stress gradually increases from the center

Table 5. Summary of the field equations, constitutive equations and boundary conditions.

Maxwell Equations:

$$\Delta\mathbf{\Phi}^m = -\mu_0 \nabla\times\mathbf{M}\ .$$

Conservation of Linear and Angular Momentum:

$$\nabla\cdot\boldsymbol{\sigma}^{MT} - \mu_0\mathbf{H}(\nabla\cdot\mathbf{M}) = \mathbf{0}\ , \quad \text{skw}(\boldsymbol{\sigma}^{MT}) = \mathbf{0}\ .$$

Constitutive Equations:

$M_y = M_y(H_y),\ M_x = M_x(H_y)$ (Response of Figure (12))

$$\boldsymbol{\sigma}^{MT} = \mathbf{C} : (\boldsymbol{\varepsilon} - \boldsymbol{\varepsilon}^{\mathbf{r}}) \in \text{Sym}$$

with $\boldsymbol{\varepsilon} = \frac{1}{2}(\nabla\mathbf{u} + \nabla\mathbf{u}^T)$, $\boldsymbol{\varepsilon}^r = \mathbf{\Lambda}\xi$ and

$$\mathbf{\Lambda} = \varepsilon^{r,max}\begin{bmatrix} 1 & 0 & 0 \\ 0 & -1 & 0 \\ 0 & 0 & 0 \end{bmatrix}\ .$$

Boundary Conditions:

$$[\![\boldsymbol{B}]\!]\cdot\boldsymbol{n} = 0, \quad [\![\boldsymbol{H}]\!]\times\boldsymbol{n} = \mathbf{0}\ ,$$

$$[\![\boldsymbol{\sigma} + \boldsymbol{\sigma}^M]\!]\cdot\mathbf{n} = \mathbf{0} \quad \text{or}$$

$$\Longrightarrow \boldsymbol{\sigma}^{MT}\mathbf{n} = \mathbf{t^a} + \tfrac{\mu_0}{\mathbf{2}}(\mathbf{M}\cdot\mathbf{n})^{\mathbf{2}}\mathbf{n} + \mu_{\mathbf{0}}(\mathbf{H}\otimes\mathbf{M})\mathbf{n}\ .$$

(a) (b)

Figure 20. (a) σ_{xx} and (b) σ_{yy}-component distribution of the Cauchy stress tensor (MPa) at an applied magnetic induction level of $\mu_0\langle H_y\rangle = 1$ T.

Table 6. Cauchy stress values (MPa) at an applied induction level of 1 T.

	P_0	P_1	P_2	P_3	P_4	P_5	P_6	P_7	P_8
σ_{xx}	-3.58	-2.31	-2.25	-2.30	-2.15	-2.32	-2.25	-2.32	-2.17
σ_{yy}	-0.39	-0.08	-0.10	-0.22	-0.11	-0.07	-0.11	-0.22	-0.11

towards the left and right edges, where the sign changes from negative to positive. Note also that the horizontal component σ_{yy} is *non-zero* and attains values of almost -0.53 MPa as observed in Figure 20(b). It is compressive in most of the sample, except regions A and B indicated in Figure 20(b), where it exhibits positive values. Except for the concentrations near the corners, the magnitude of the σ_{yy} component is high around the center, where it reaches the compressive stress of largest magnitude with -0.39 MPa, and then decreases towards the edges.

Table 7. Percentage difference in the computed local Cauchy stresses and a homogeneous stress level of -2.0MPa at an applied induction of 1 T.

	P_0	P_1	P_2	P_3	P_4	P_5	P_6	P_7	P_8
σ_{xx}	79.0	15.5	12.5	15.0	7.5	16.0	12.5	16.0	8.5

It is interesting to realize that if magnetic body forces and couples are taken into account, the traction boundary conditions are also influenced by the magnetic

(a) (b)

Figure 21. Variation of the mechanical traction components on $\partial\Omega_2$ and $\partial\Omega_4$ at $\mu_0\langle H_y\rangle = 1$ T (a) x-components and (b) y-components.

field variables. The traction $\mathbf{t}^a$ is related to the Cauchy's formula by $\boldsymbol{\sigma}\mathbf{n} = \mathbf{t}^a$. When Maxwell stress is considered along with the Cauchy stress, an additional magneto-traction is generated. The combined traction can be calculated [69] from the jump condition $\left[\boldsymbol{\sigma}+\boldsymbol{\sigma}^M\right]\mathbf{n} = \mathbf{0}$. Since the *mechanical part* $\boldsymbol{\sigma}^{MT}$ of the Cauchy stress is linked with the total strain through the constitutive equation (23), we switched our reference stress $\boldsymbol{\sigma}$ to the symmetric mechanical stress $\boldsymbol{\sigma}^{MT}$ to solve the coupled problem. Due to this switching, the traction boundary condition modified by $\tilde{\mathbf{t}} = \boldsymbol{\sigma}^{MT}\mathbf{n}$, which is related to $\mathbf{t}^a$ through the expression (A13). We can write

$$\tilde{\mathbf{t}}_{\partial\Omega_1} = (-2 + \mu_0 M_x H_x + \frac{\mu_0}{2} M_x^2)\mathbf{e}_x + \mu_0 M_x H_y \mathbf{e}_y \ , \tag{26a}$$

$$\tilde{\mathbf{t}}_{\partial\Omega_2} = \mu_0 M_y H_x \mathbf{e}_x + (\mu_0 M_y H_y + \frac{\mu_0}{2} M_y^2)\mathbf{e}_y \ , \tag{26b}$$

$$\tilde{\mathbf{t}}_{\partial\Omega_3} = -\mu_0 M_x H_y \mathbf{e}_y \ , \tag{26c}$$

$$\tilde{\mathbf{t}}_{\partial\Omega_4} = -\mu_0 M_y H_x \mathbf{e}_x + (-M_y H_y - \frac{\mu_0}{2} M_y^2)\mathbf{e}_y \ . \tag{26d}$$

It should be noted that the x-component of the traction in Eq. (26c) on $\partial\Omega_3$ is not imposed since the displacement boundary condition is given. At $\mu_0\langle H_y\rangle = 1$ T the variant reorientation process is almost complete and the M_x component is almost zero, as we explained in the previous section. So, the traction on the boundary segments $\partial\Omega_1$ and $\partial\Omega_3$ are $\tilde{t}_{x,\partial\Omega_1} \approx -2$ MPa and $\tilde{t}_{y,\partial\Omega_3} \approx 0$ MPa, respectively. The variation of the x-component of $\tilde{\mathbf{t}}$ on $\partial\Omega_2$ and $\partial\Omega_4$ is plotted in Fig. 21(a). It ranges from -0.6 MPa to 0.6 MPa and the two curves coincide at each end point due to point-symmetric behavior of H_x. The variation of the y-component $\tilde{\mathbf{t}}$ on the segments $\partial\Omega_2$ and $\partial\Omega_4$ is displayed in Fig. 21(b). In this case its magnitude exceeds 1.0 MPa.

7. Conclusions

In this paper magnetostatic and magneto-mechanically-coupled finite element analysis involving nonlinear magnetic shape memory behavior was presented. To the authors' knowledge simulations of this kind have not been reported elsewhere in the literature. Based on this analysis two important effects that substantially influence the constitutive modeling of MSMAs have been addressed. First, it was shown that magnetostatic computations could be used to properly account for the shape-dependent demagnetization effect which complicates the model parameter identification from experimental data. It was pointed out that this must be understood as the *inverse problem* of finding the model parameters such that the simulation results in the applied magnetic field vs. magnetization curve measured in the experiment for a specific sample geometry. An iterative procedure was established for which in each iteration step the magnetostatic boundary value problem was solved to obtain the relation between the applied and internal magnetic fields needed to correct the data. Furthermore, a parametric study of the specimen as-

pect ratio dependence on the demagnetization effect was presented. It was found that, although the demagnetization effect varies with aspect ratio, it has significant influence on the measured magnetization curves for any aspect ratio and must certainly be accounted for. In case only average quantities are of interest, it was shown that the commonly applied demagnetization factor methodology yields sufficiently accurate results, provided, of course, the factor is available for the considered geometry. If, however, the local distribution of the field quantities in non-ellipsoidal specimen must be investigated, for example, to identify possible magnetic field and stress peaks or to investigate the influence of cracks, inclusions or other inhomogeneities, this can only be achieved via the numerical solution of coupled boundary value problems as presented in this paper.

The second main effort of the presented work was concerned with the investigation of the significance of magnetic body forces and body couples and whether or not these can be neglected in the modeling of MSMAs. In a first estimate of this influence, highly non-uniform distributions of the magnetic body force and couple and consequently the Maxwell stress field were computed from the nonlinear magnetostatic finite element analysis in a post-processing manner. In a second step, an extended analysis based on the numerical solution of the magneto-mechanically-coupled problem then revealed that the magnetic body force and body couple cause an inhomogeneous Cauchy stress field, whose components are comparable to the typically applied stresses. This suggests that, considering current blocking stress levels, the influence of body forces should not be neglected.

From the analysis presented in this paper further challenges emerge for possible future work. Most importantly, the proposed methodology should be implemented for three-dimensional simulations and fully-coupled FE-analysis. The later would involve accounting for the change in the magnetization response with changes in the stress level, which are captured in the Kiefer & Lagoudas constitutive model, but have been so far neglected in the boundary value problem computations. An interesting question that then arises is whether the phenomenological model equations should be based on the Cauchy stress or rather the total stress tensor as an independent state variable and which of these quantities is actually measured in experiments.

Acknowledgments

The authors would like to acknowledge the financial support of the Army Research Office, Grant no. W911NF-06-1-0319 and the financial support of NSF-IIMEC (International Institute for Multifunctional Materials for Energy Conversion) under Grant No. DMR-0844082.

APPENDIX

Appendix A. Magneto Mechanical Boundary Conditions

We seek to prove that if

$$[\![\boldsymbol{\sigma} + \boldsymbol{\sigma}^M]\!]\mathbf{n} = \mathbf{0}\ , \tag{A1}$$

then

$$\boldsymbol{\sigma}^{MT}\mathbf{n} = \mathbf{t}^a + \mu_0(\mathbf{H}\otimes\mathbf{M})\mathbf{n} + \frac{\mu_0}{2}(\mathbf{M}\cdot\mathbf{n})^2\mathbf{n}\ , \tag{A2}$$

where $\boldsymbol{\sigma}\mathbf{n} = \mathbf{t}^a$. Therein, $\mathbf{n}$ is the outward unit normal to the boundary $\partial\Omega$ and $[\![A]\!] := A^+ - A^-$ is the jump operator, where A^+ and A^- represent the values of A on either side of the discontinuity surface. From Ampère's law, we can conclude that $[\![\mathbf{H}^t]\!] = 0$, i.e. Eq. 2(b), where the superscript t represents the tangential direction. It then follows $\mathbf{H} = \mathbf{H}^n + \mathbf{H}^t = (\mathbf{H}\cdot\mathbf{n})\mathbf{n} + \mathbf{H}^t$ and

$$[\![\mathbf{H}]\!] = [\![\mathbf{H}^n]\!] + [\![\mathbf{H}^t]\!] = [\![\mathbf{H}^n]\!] = ([\![\mathbf{H}]\!]\cdot\mathbf{n})\mathbf{n}\,. \tag{A3}$$

Using the constitutive relation $\mathbf{H} = \frac{1}{\mu_0}\mathbf{B} - \mathbf{M}$ in Eq. (A3) and Eq. (2a) we find

$$\begin{aligned}[\![\mathbf{H}]\!] &= (\frac{1}{\mu_0}[\![\mathbf{B}]\!]\cdot\mathbf{n} - [\![\mathbf{M}]\!]\cdot\mathbf{n})\mathbf{n}\\ &= -([\![\mathbf{M}]\!]\cdot\mathbf{n})\mathbf{n}\\ &= -[(\mathbf{M}^+ - \mathbf{M}^-)\cdot\mathbf{n}]\mathbf{n}\\ &= (\mathbf{M}\cdot\mathbf{n})\mathbf{n}\,.\end{aligned} \tag{A4}$$

Here we have used the fact that $\mathbf{M}^+ = 0$ and $\mathbf{M}^- = \mathbf{M}$. Note that Eq. (15) can be rewritten as $\boldsymbol{\sigma}^M = \mathbf{H}\otimes\mathbf{B} - \frac{\mu_0}{2}(\mathbf{H}\cdot\mathbf{H})\mathbf{I}$. It follows that

$$\begin{aligned}[\![\boldsymbol{\sigma}^M]\!]\mathbf{n} &= [\![\mathbf{H}\otimes\mathbf{B}]\!]\mathbf{n} - \frac{\mu_0}{2}[\![(\mathbf{H}\cdot\mathbf{H})\mathbf{I}]\!]\mathbf{n} \qquad (A5)\\ &= (\mathbf{H}^+\otimes\mathbf{B}^+ - \mathbf{H}^-\otimes\mathbf{B}^-)\mathbf{n} - \frac{\mu_0}{2}(\mathbf{H}^+\cdot\mathbf{H}^+ - \mathbf{H}^-\cdot\mathbf{H}^-)\mathbf{n}.\end{aligned}$$

The first term in Eq. (A5), using $[\![\mathbf{B}]\!]\cdot\mathbf{n} = (\mathbf{B}^+\cdot\mathbf{n}) - (\mathbf{B}^-\cdot\mathbf{n}) = 0$, may be written as

$$\begin{aligned}(\mathbf{H}^+\otimes\mathbf{B}^+ - \mathbf{H}^-\otimes\mathbf{B}^-)\mathbf{n} &= (\mathbf{B}^+\cdot\mathbf{n})\mathbf{H}^+ - (\mathbf{B}^-\cdot\mathbf{n})\mathbf{H}^-\\ &= (\mathbf{B}^+\cdot\mathbf{n})(\mathbf{H}^+ - \mathbf{H}^-)\\ &= (\mathbf{B}^+\cdot\mathbf{n})[\![\mathbf{H}]\!]\end{aligned} \tag{A6}$$

From Eq. (2b) it is clear that $[\![\mathbf{H}^t]\!] = [\![\mathbf{n}\times\mathbf{H}]\!] = \mathbf{0}$ and consequently $[\![\mathbf{H}^t\cdot\mathbf{H}^t]\!] = 0$ implies (cf. [69]),

$$|\mathbf{n}\times\mathbf{H}^+|^2 = |\mathbf{n}\times\mathbf{H}^-|^2 \tag{A7}$$

Using the identity $(\mathbf{a}\times\mathbf{b})\cdot(\mathbf{c}\times\mathbf{d}) = (\mathbf{a}\cdot\mathbf{c})(\mathbf{b}\cdot\mathbf{d}) - (\mathbf{a}\cdot\mathbf{d})(\mathbf{b}\cdot\mathbf{c})$, we can write

$$(\mathbf{n}\times\mathbf{H}^+)\cdot(\mathbf{n}\times\mathbf{H}^+) = (\mathbf{n}\cdot\mathbf{n})(\mathbf{H}^+\cdot\mathbf{H}^+) - (\mathbf{H}^+\cdot\mathbf{n})^2\,. \tag{A8}$$

Similarly,

$$(\mathbf{n}\times\mathbf{H}^-)\cdot(\mathbf{n}\times\mathbf{H}^-) = (\mathbf{n}\cdot\mathbf{n})(\mathbf{H}^-\cdot\mathbf{H}^-) - (\mathbf{H}^-\cdot\mathbf{n})^2\,. \tag{A9}$$

From Eqs. (A7), (A8) and (A9), we conclude

$$|\mathbf{H}^+|^2 - (\mathbf{H}^+\cdot\mathbf{n})^2 = |\mathbf{H}^-|^2 - (\mathbf{H}^-\cdot\mathbf{n})^2\,. \tag{A10}$$

which means $[\![\mathbf{H}\cdot\mathbf{H}]\!] = [\![(\mathbf{H}\cdot\mathbf{n})^2]\!]$. Now with Eq. (A10) we can write the second term on the right hand side of Eq. (A5) in the following form

$$\begin{aligned}\frac{\mu_0}{2}[\mathbf{H}^+\cdot\mathbf{H}^+ - \mathbf{H}^-\cdot\mathbf{H}^-]\mathbf{n} &= \frac{\mu_0}{2}[(\mathbf{H}^+\cdot\mathbf{n})^2 - (\mathbf{H}^-\cdot\mathbf{n})^2]\mathbf{n} \\ &= \frac{\mu_0}{2}[(\mathbf{H}^+ - \mathbf{H}^-)\cdot\mathbf{n}][(\mathbf{H}^+ + \mathbf{H}^-)\cdot\mathbf{n}]\mathbf{n}\ .\end{aligned}$$

Considering that $(\mathbf{H}^+ - \mathbf{H}^-)\cdot\mathbf{n} = [\![\mathbf{H}]\!]\cdot\mathbf{n}$ and $(\mathbf{H}^+ + \mathbf{H}^-)\cdot\mathbf{n} = [(\frac{1}{\mu_0}\mathbf{B}^+ - \mathbf{M}^+) + (\frac{1}{\mu_0}\mathbf{B}^- - \mathbf{M}^-)]\cdot\mathbf{n} = [\frac{1}{\mu_0}\mathbf{B}^+ + \frac{1}{\mu_0}\mathbf{B}^- - \mathbf{M}^-]\cdot\mathbf{n}$, with $\mathbf{B}^+\cdot\mathbf{n} = \mathbf{B}^-\cdot\mathbf{n}$ due to Eq. (2a) and Eq. (A4), it follows

$$\begin{aligned}\frac{\mu_0}{2}[\mathbf{H}^+\cdot\mathbf{H}^+ - \mathbf{H}^-\cdot\mathbf{H}^-]\mathbf{n} &= \frac{\mu_0}{2}[\![\mathbf{H}]\!]\cdot\mathbf{n}[\frac{2}{\mu_0}(\mathbf{B}^+ - \mathbf{M})\cdot\mathbf{n}]\mathbf{n} \\ &= (\mathbf{B}^+\cdot\mathbf{n})([\![\mathbf{H}]\!]\cdot\mathbf{n})\mathbf{n} - \frac{\mu_0}{2}(\mathbf{M}\cdot\mathbf{n})([\![\mathbf{H}]\!]\cdot\mathbf{n})\mathbf{n} \\ &= (\mathbf{B}^+\cdot\mathbf{n})[\![\mathbf{H}]\!] - \frac{\mu_0}{2}(\mathbf{M}\cdot\mathbf{n})[\![\mathbf{H}]\!] \\ &= (\mathbf{B}^+\cdot\mathbf{n})[\![\mathbf{H}]\!] - \frac{\mu_0}{2}(\mathbf{M}\cdot\mathbf{n})^2\mathbf{n}\ . \qquad \text{(A11)}\end{aligned}$$

Substitution of Eqs. (A6) and (A11) into Eq. (A5) yields

$$[\![\boldsymbol{\sigma}^M]\!]\mathbf{n} = \frac{\mu_0}{2}(\mathbf{M}\cdot\mathbf{n})^2\mathbf{n}\ . \qquad \text{(A12)}$$

In consequence, with Eq. (20), we obtain

$$\begin{aligned}[\![\boldsymbol{\sigma} + \boldsymbol{\sigma}^M]\!]\mathbf{n} &= [\![\boldsymbol{\sigma}]\!]\mathbf{n} + [\![\boldsymbol{\sigma}^m]\!]\mathbf{n} \\ &= (\boldsymbol{\sigma}^+ - \boldsymbol{\sigma}^-)\mathbf{n} + [\![\boldsymbol{\sigma}^m]\!]\mathbf{n} \\ &= \mathbf{t}^a - \boldsymbol{\sigma}\mathbf{n} + \frac{\mu_0}{2}(\mathbf{M}\cdot\mathbf{n})^2\mathbf{n} \\ &= \mathbf{t}^a - \boldsymbol{\sigma}^{MT}\mathbf{n} + \mu_0(\mathbf{H}\otimes\mathbf{M})\mathbf{n} + \frac{\mu_0}{2}(\mathbf{M}\cdot\mathbf{n})^2\mathbf{n}\ .\end{aligned}$$

Finally, Eq. (A1) yields the boundary condition in the following form

$$\boxed{\boldsymbol{\sigma}^{MT}\mathbf{n} = \mathbf{t}^a + \mu_0(\mathbf{H}\otimes\mathbf{M})\mathbf{n} + \tfrac{\mu_0}{2}(\mathbf{M}\cdot\mathbf{n})^2\mathbf{n}} \qquad \text{(A13)}$$

References

[1] B. Kiefer and D.C. Lagoudas, Philosophical Magazine Special Issue: Recent Advances in Theoretical Mechanics 85 (2005) p. 4289–4329.
[2] T. Yamamoto, M. Taya, Y. Sutou, Y. Liang, T. Wada and L. Sorensen, Acta Materialia 52 (2004) p. 5083–5091.
[3] O. Heczko, L. Straka and K. Ullakko, Journal de Physique IV France 112 (2003) p. 959–962.
[4] R.C. O'Handley, Journal of Applied Physics 83 (1998) p. 3263–3270.
[5] R.C. O'Handley, S.J. Murray, M. Marioni, H. Nembach and S.M. Allen, Journal of Applied Physics 87 (2000) p. 4712–4717.
[6] S.J. Murray, M. Marioni, P.G. Tello, S.M. Allen and R.C. O'Handley, Journal of Magnetism and Magnetic Materials 226–230 (2001) p. 945–947.
[7] P. Müllner, V.A. Chernenko and G. Kostorz, Journal of Magnetism and Magnetic Materials 267 (2003) p. 325–334.
[8] T.W. Shield, Review of Scientific Instruments 74 (2003) p. 4077–4088.
[9] A.A. Likhachev, A. Sozinov and K. Ullakko, Material Science & Engineering A 378 (2004) p. 513–518.

[10] M. Pasquale, Sensors and Actuators A 106 (2003) p. 142–148.
[11] J. Tellinen, I. Suorsa, I. Jääskeläinen Aaltio and K. Ullakko, in: Proceedings of the 8th International Conference ACTUATOR 2002, Bremen, Germany, 10-12 June 2002 (2002) p. 566–569.
[12] N. Sarawate and M. Dapino, Applied Physics Letters 88 (2006) p. 121923.
[13] N.N. Sarawate and M.J. Dapino, Journal of Applied Physics 101 (2007) p. 123522.
[14] R. Tickle and R.D. James, Journal of Magnetism and Magnetic Materials 195 (1999) p. 627–638.
[15] O. Heczko, A. Sozinov and K. Ullakko, IEEE Transactions on Magnetics 36 (2000) p. 3266–3268.
[16] P. Müllner, V.A. Chernenko, M. Wollgarten and Kostorz, Journal of Applied Physics 92 (2002) p. 6708–6713.
[17] H.E. Karaca, I. Karaman, B. Basaran, Y.I. Chumlyakov and H.J. Maier, Acta Materialia 54 (2006) p. 233–245.
[18] P.J. Webster, K.R.A. Ziebeck, S.L. Town and M.S. Peak, Philosophical Magazine B 49 (1984) p. 295–310.
[19] I.K. Zasimchuk, V.V. Kokorin, V.V. Martynov, A.V. Tkachenko and V.A. Chernenko, Physics of Metals and Metallography 69 (1990) p. 104–108.
[20] V.V. Martynov and V.V. Kokorin, Journal de Physique III France 2 (1992) p. 739–749.
[21] K. Ullakko, J.K. Huang, C. Kantner, R.C. O'Handley and V.V. Kokorin, Applied Physics Letters 69 (1996) p. 1966–1968.
[22] J. Cui, T.W. Shield and R.D. James, Acta Materialia 52 (2004) p. 35–47.
[23] R.D. James and M. Wuttig, Philosophical Magazine A 77 (1998) p. 1273–1299.
[24] S.J. Murray, R. Hayashi, M. Marioni, S.M. Allen and R.C. O'Handley, Proceedings of SPIE 3675 (1999) p. 204–211.
[25] A. Fujita, K. Fukamichi, F. Gejima, R. Kainuma and K. Ishida, Applied Physics Letters 77 (2000) p. 3054–3056.
[26] T. Kakeshita, T. Takeuchi, T. Fukuda, M. Tsujiguchi, T. Saburi, R. Oshima and S. Muto, Applied Physics Letters 77 (2000) p. 1502–1504.
[27] M. Wuttig, L. Liu, K. Tsuchiya and R.D. James, Journal of Applied Physics 87 (2000) p. 4707–4711.
[28] M. Wuttig, J. Li and C. Craciunescu, Scripta Materialia 44 (2001) p. 2393–2397.
[29] A. Sozinov, A.A. Likhachev, N. Lanska, O. Söderberg, K. Ullakko and V.K. Lindroos, in: Proceedings of SPIE, Symposium on Smart Structures and Materials 5053 (2003) p. 586–594.
[30] H.E. Karaca, I. Karaman, D.C. Lagoudas, H.J. Maier and Y.I. Chumlyakov, Scripta Materialia 49 (2003) p. 831–836.
[31] H. Morito, A. Fujita, R. Kainuma, K. Ishida and K. Oikawa, Applied Physics Letters 81 (2002) p. 1657–1659.
[32] B. Kiefer, *A Phenomenological Constitutive Model for Magnetic Shape Memory Alloys*, Ph.D. dissertation, Department of Aerospace Engineering, Texas A&M University, College Station, TX, 2006.
[33] J. Kiang and L. Tong, Journal of Magnetism and Magnetic Materials 292 (2005) p. 394–412.
[34] A. DeSimone and R.D. James, Journal of Applied Physics 81 (1997) p. 5706–5708.
[35] A. DeSimone and R. James, Journal of the Mechanics and Physics of Solids 50 (2002) p. 283–320.
[36] A. DeSimone and R.D. James, Journal de Physique 112 (2003) p. 969–972.
[37] S.J. Murray, R.C. O'Handley and S.M. Allen, Journal of Applied Physics 89 (2001) p. 1295–1301.
[38] A.A. Likhachev and K. Ullakko, Physics Letters A 275 (2000) p. 142–151.
[39] L. Hirsinger and C. Lexcellent, Journal of Magnetism and Magnetic Materials 254–255 (2003) p. 275–277.
[40] L. Hirsinger and C. Lexcellent, Journal de Physique IV France 112 (2003) p. 977–980.
[41] B. Kiefer and D.C. Lagoudas, Proceedings of SPIE: Smart Structures and Materials 5387 (2004) p. 164–176.
[42] B. Kiefer and D.C. Lagoudas, *Modeling of Magnetic SMAs*, in *Introduction to Modeling and Engineering Applications of Shape Memory Alloys*, , in *Introduction to Modeling and Engineering Applications of Shape Memory Alloys*, ed. D.C. LagoudasD.C. Lagoudas ed., Springer-Verlag, New York, 2008, pp. 325–393.
[43] B. Kiefer and D.C. Lagoudas, Journal of Intelligent Material Systems and Structures 20 (2009) p. 143–170.
[44] B. Kiefer, H.E. Karaca, D.C. Lagoudas and I. Karaman, Journal of Magnetism and Magnetic Materials 312 (2007) p. 164–175.
[45] B. Kiefer and D. Lagoudas, Proceedings of SPIE: Smart Structures and Materials 6170 (2006) p. 330–341.
[46] D.C. Lagoudas, B. Kiefer and A.J. Broederdorf, Proceedings of ASME, International Mechanical Engineering Congress and Exposition, Chicago, IL, 5–10 November 2006 IMECE2006-15296 (2006) p. 311–321.
[47] K. Haldar, G. Chatzigeorgiou and D.C. Lagoudas, Journal of Intelligent Material Systems and Structures 21 (2010) p. 1103–1116.
[48] L.E. Faidley, M.J. Dapino, G.N. Washington and T.A. Lograsso, in: Proceedings of SPIE, Smart Structures and Materials: Active Materials: Behavior and Mechanics, San Diego, CA, 6–10 March 2005. Vol. 5761 (2005) p. 501–512.
[49] H. Tan and M.H. Elahinia, Submitted to Elsevier May 2006 (2006).
[50] R.C. O'Handley, S.M. Allen, D.I. Paul, C.P. Henry, M. Marioni, D. Bono, C. Jenkins, A. Banful and R. Wager, Proceedings of SPIE 5053 (2003) p. 200–206.
[51] Y. Liang, H. Kato and M. Taya, Mechanics of Materials 38 (2006) p. 564–570.
[52] J.D. Jackson, *Classical Electrodynamics*, 2nd John Wiley & Sons, New York, 1975.
[53] H.H. Woodson and J.R. Melcher, *Electromechanical Dynamics, Part I: Discrete Systems*, Reprint of 1968 Krieger Publishing Company, Malabar, FL, 1990.
[54] M.R. Sullivan and H.D. Chopra, Physical Review B 70 (2004) p. 094427–(1–8).
[55] R.C. O'Handley, S.M. Allen, D.I. Paul, C.P. Henry, M. Marioni, D. Bono, C. Jenkins, A. Banful and R. Wager, in: Proceedings of SPIE, Symposium on Smart Structures and Materials 5053 (2003) p.

200–206.
[56] R. Tickle, *Ferromagnetic Shape Memory Materials*, University of Minnesota, Minneapolis, MN, 2000.
[57] B.D. Cullity, *Introduction to Magnetic Materials*, Addison-Wesley, Reading, MA, 1972.
[58] H.N. Bertram, *Theory of Magnetic Recording*, Cambridge University Press, Cambridge, UK, 1994.
[59] E. Schlömann, Journal of Applied Physics 33 (1962) p. 2825–2826.
[60] R.C. O'Handley, *Modern Magnetic Materials*, John Wiley & Sons, New York, 2000.
[61] R.M. Bozorth, *Ferromagnetism*, Reissue of 1951 IEEE Press, 1993.
[62] J.D. Eshelby, Proceedings of the Royal Society of London. Series A, Mathematical and Physical Sciences 241 (1957) p. 376–396.
[63] T. Mura, *Micromechanics of Defects in Solids*, 2nd revised , Mechanics of Elastic and Inelastic Solids Kluwer Academic Publisher, Dordrecht, The Netherlands, 1987.
[64] R. Moskowitz and E. Della Torre, IEEE Transactions on Magnetics 2 (1966) p. 739–744.
[65] H. Fukushima, Y. Nakatani and N. Hayashi, IEEE Transactions on Magnetics 34 (1998) p. 193–198.
[66] K. Hutter and A.A.F. Venvan de , *Field Matter Interactions in Thermoelastic Solids*, Lecture Notes in Physics Vol. 88, Springer-Verlag, New York, 1978.
[67] A.C. Eringen and G.A. Maugin, *Electrodynamics of Continua I — Foundations and Solid Media*, Springer-Verlag, New York, 1990.
[68] S.J. Murray, M. Marioni, S.M. Allen and R.C. O'Handley, Applied Physics Letters 77 (2000) p. 886–888.
[69] D.J. Steigmann., Non-Linear Mechanics 39 (2004) p. 1193–1216.

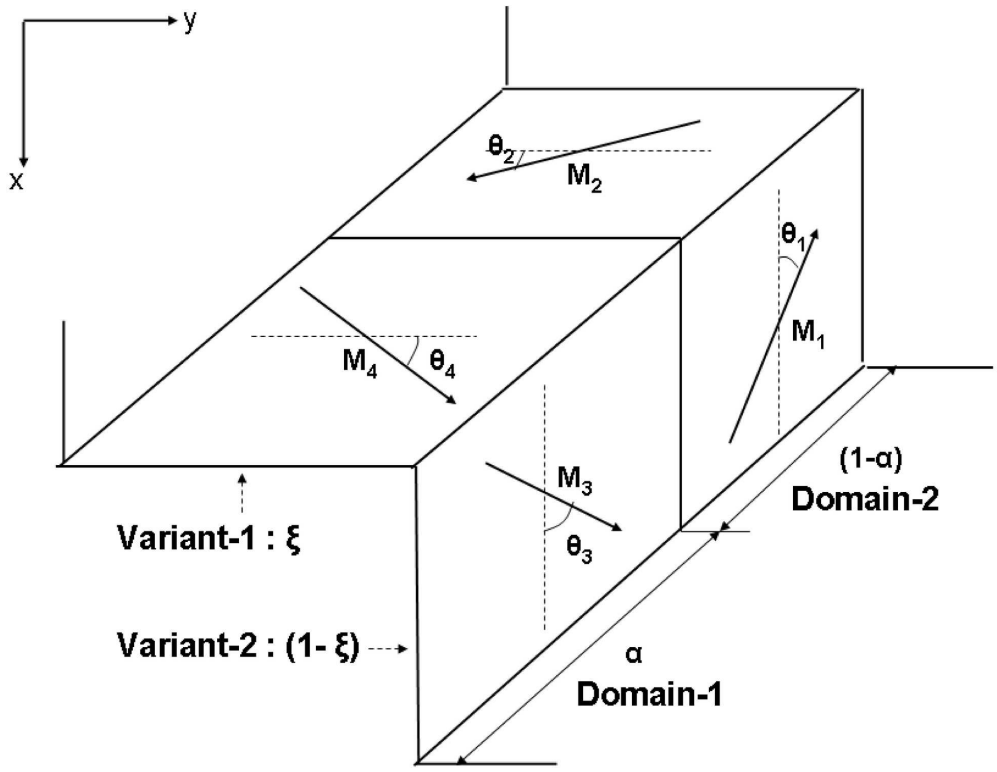

Figure 1
166x127mm (300 x 300 DPI)

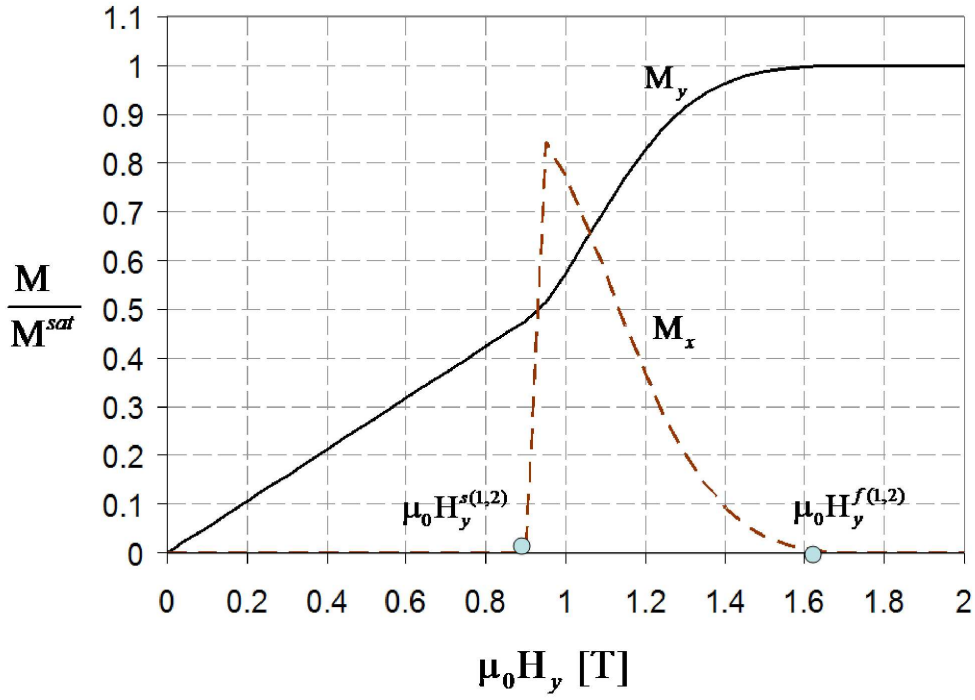

Figure 2
254x190mm (600 x 600 DPI)

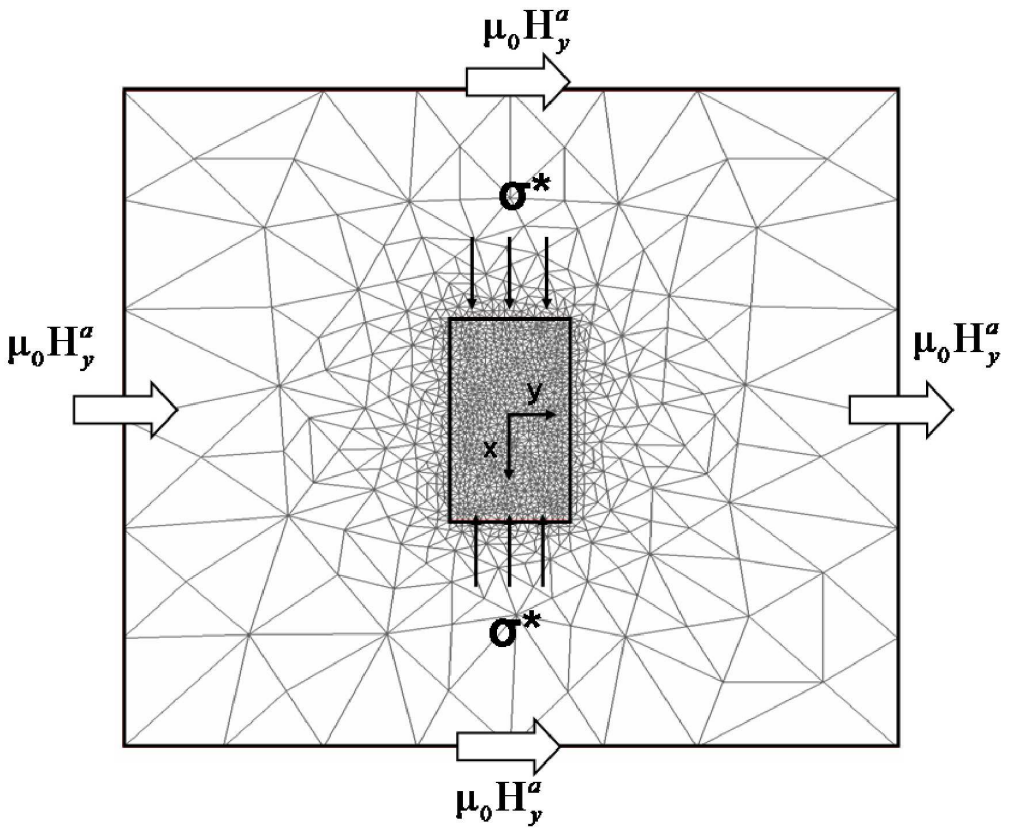

Figure 3
220x182mm (600 x 600 DPI)

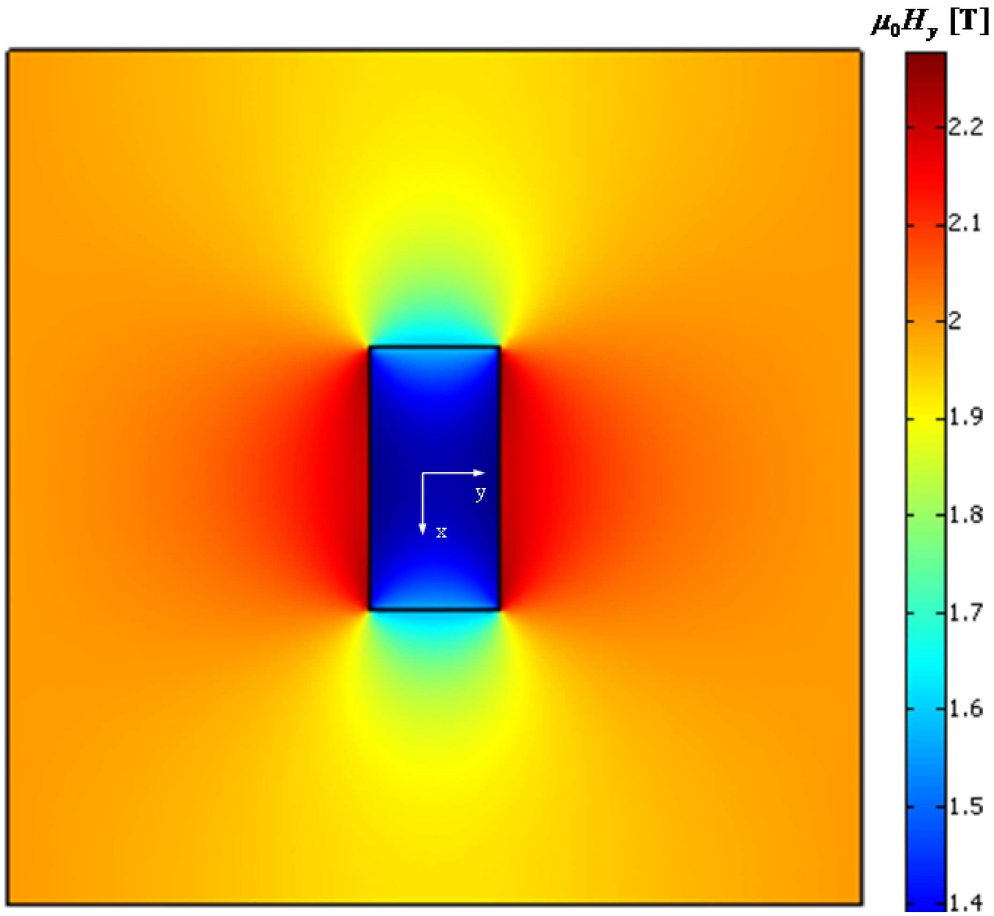

Figure 4
181x165mm (600 x 600 DPI)

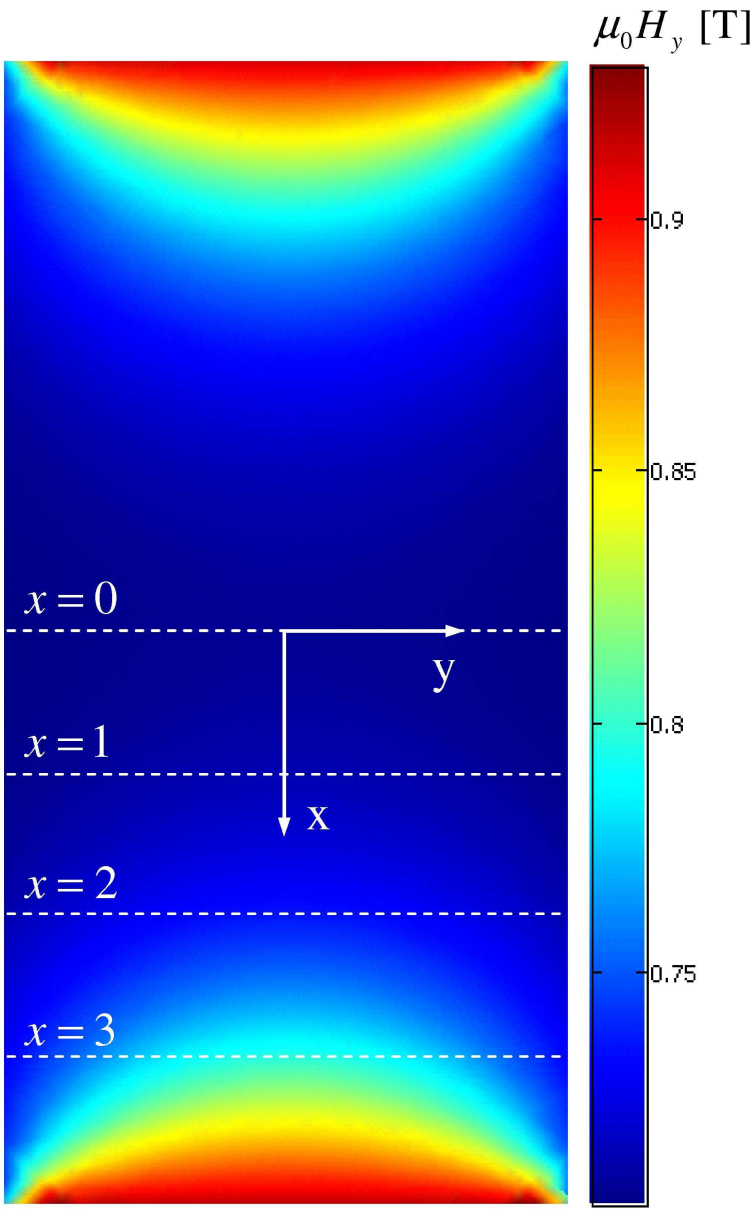

Figure 5(a)
87x138mm (600 x 600 DPI)

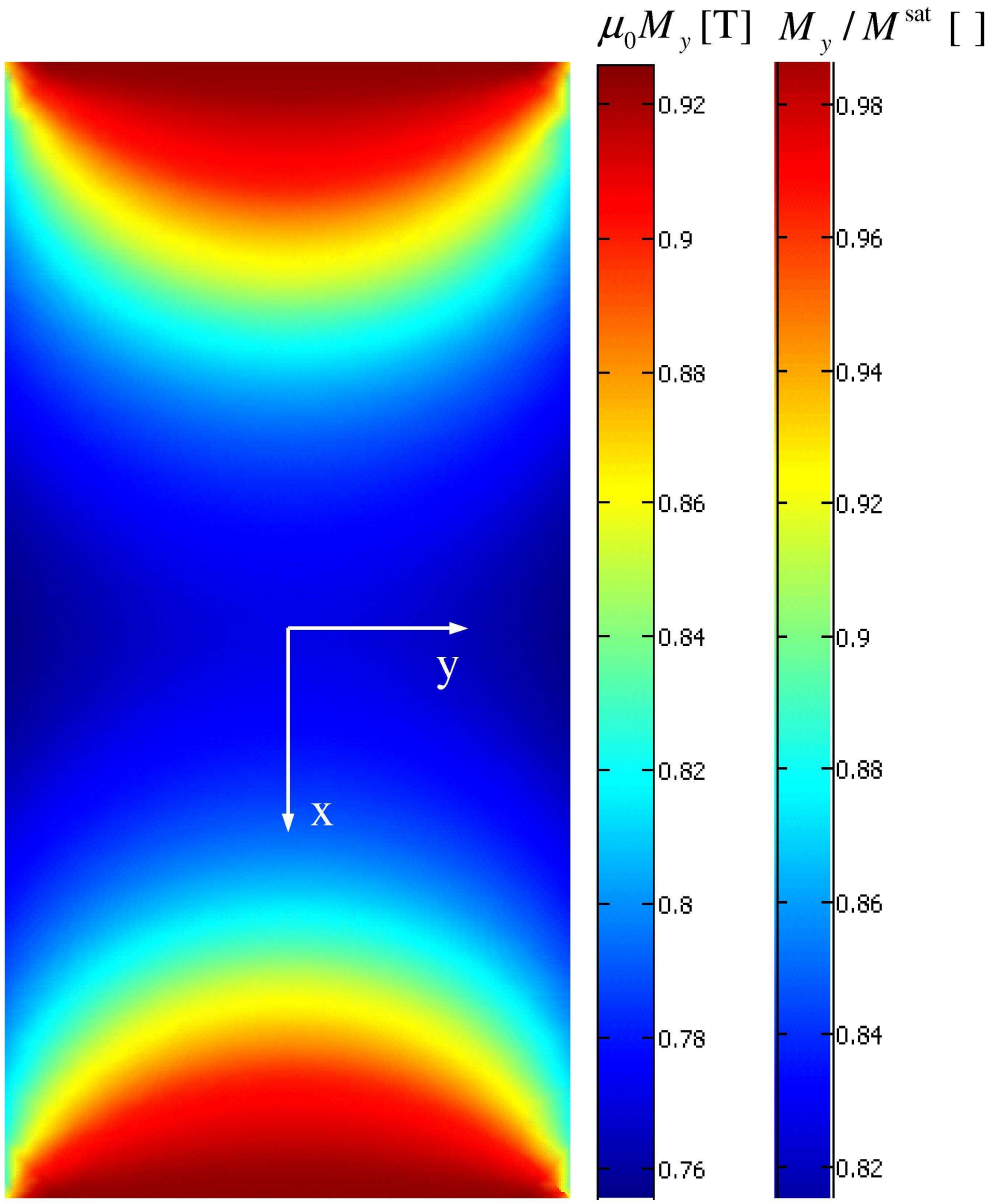

Figure 5(b)
114x138mm (600 x 600 DPI)

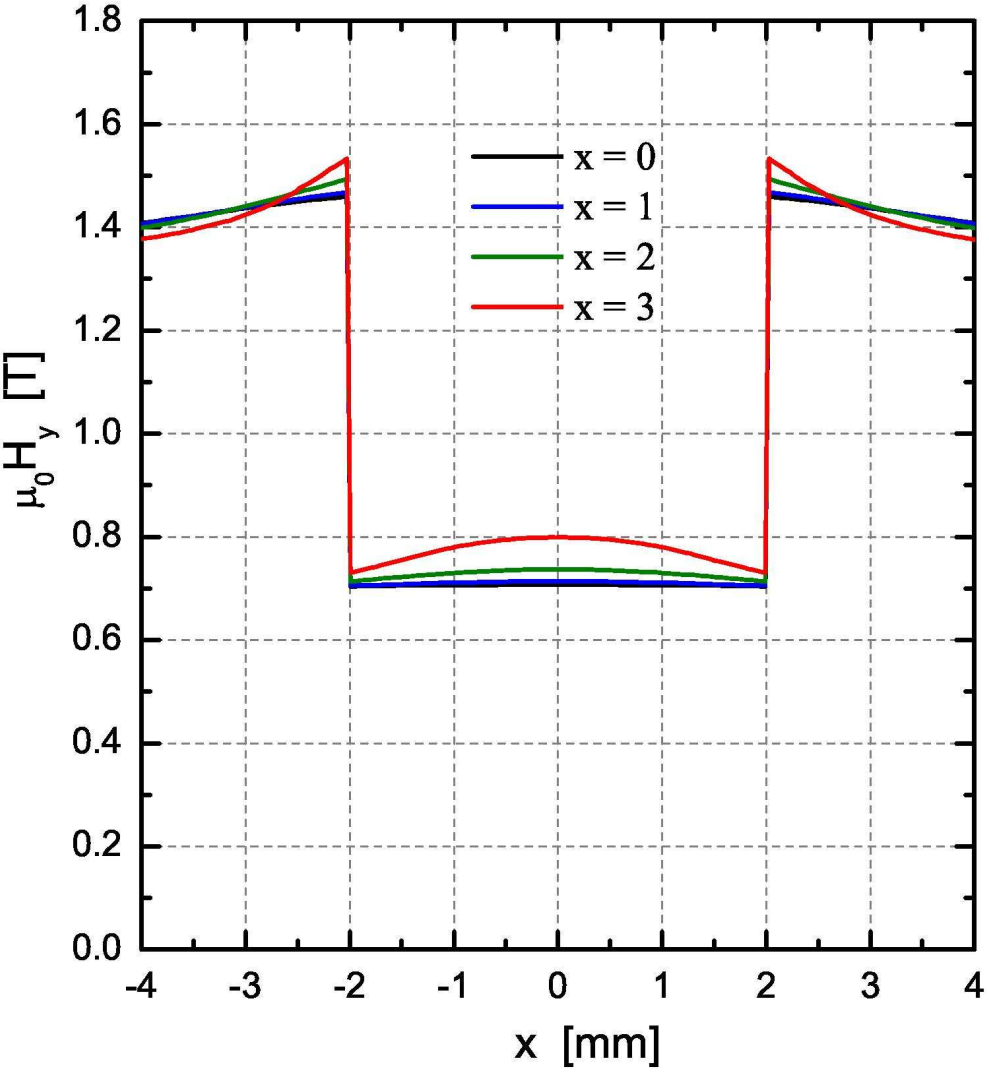

Figure 6(a)
64x69mm (600 x 600 DPI)

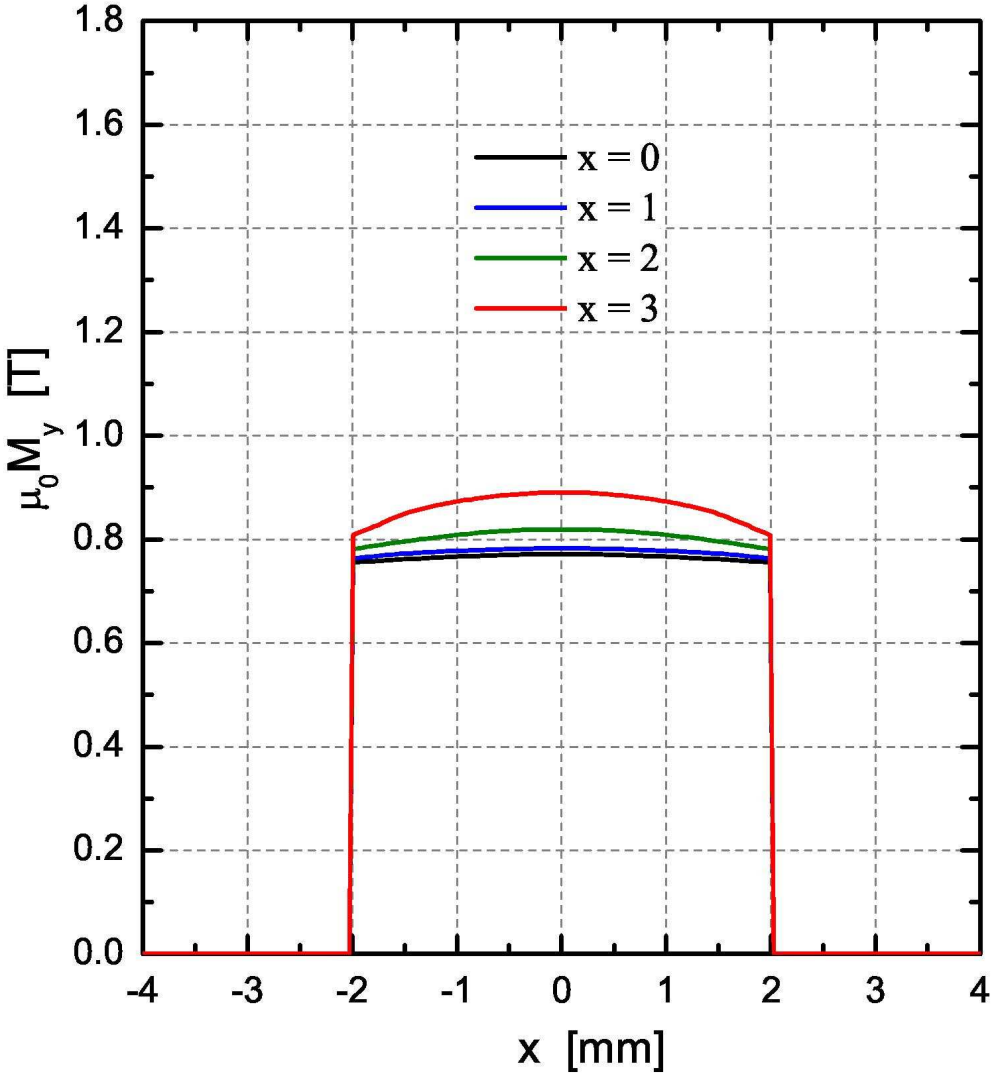

Figure 6(b)
63x69mm (600 x 600 DPI)

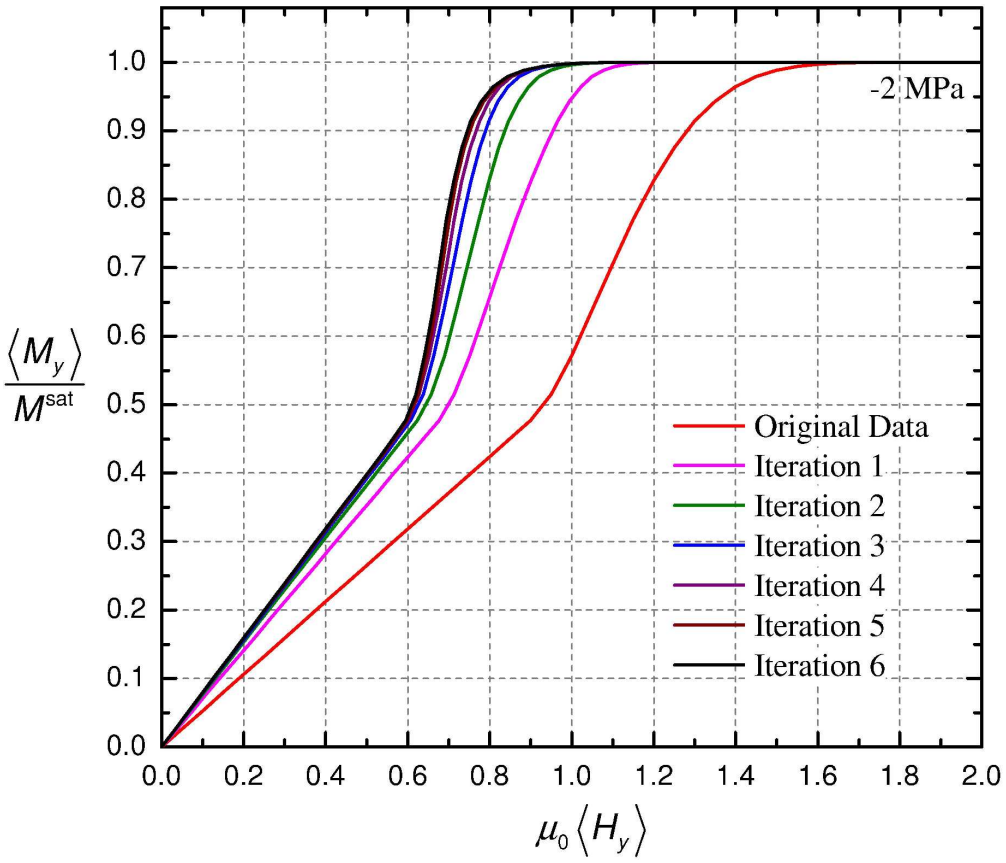

Figure 7
155x132mm (600 x 600 DPI)

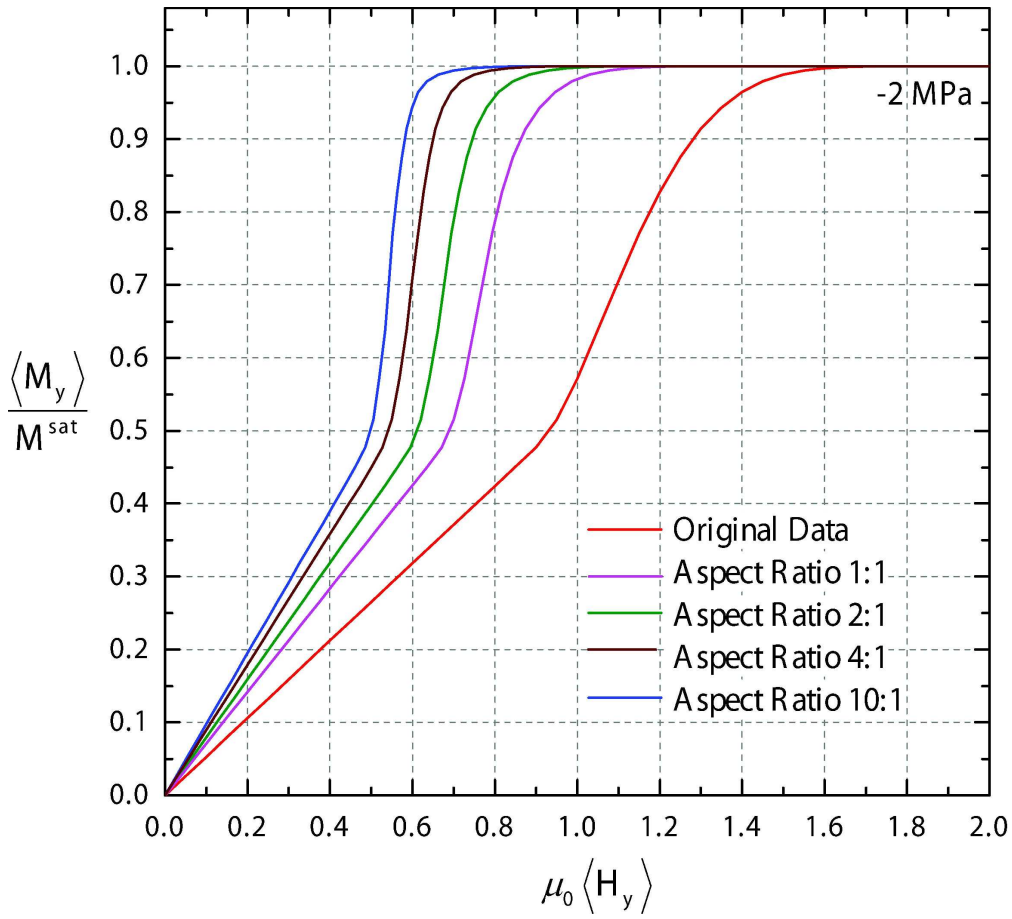

Figure 8
196x178mm (600 x 600 DPI)

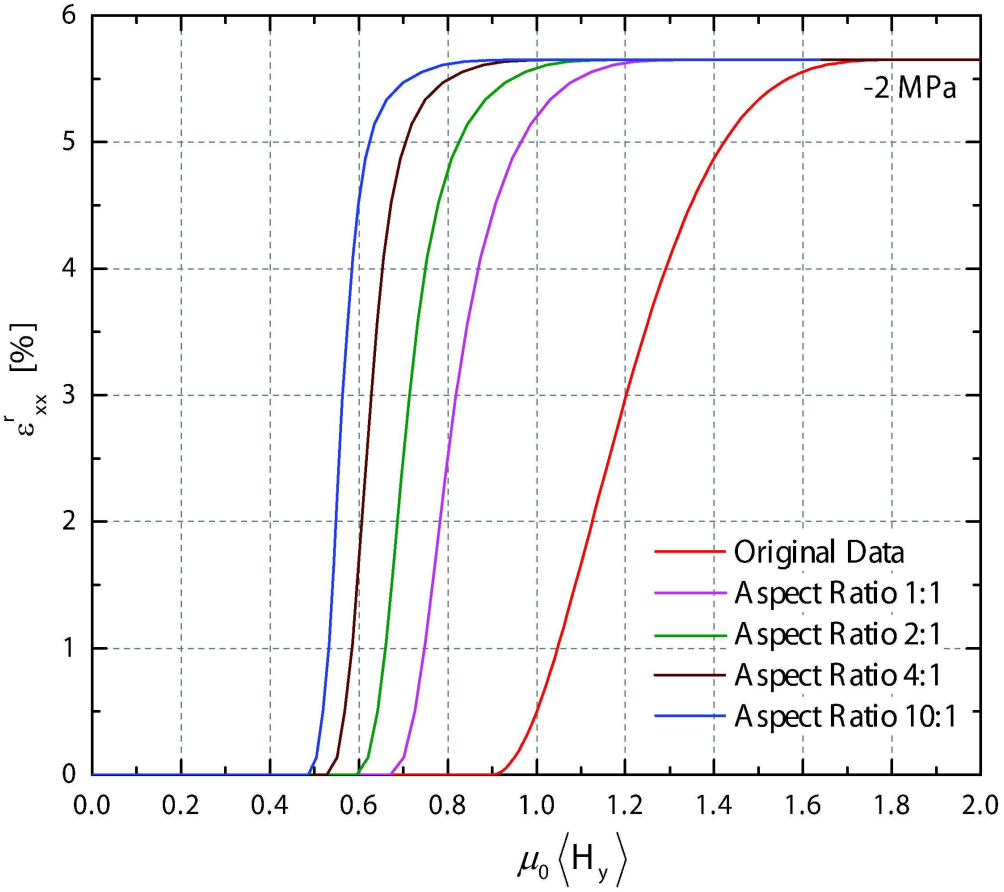

Figure 9
189x169mm (600 x 600 DPI)

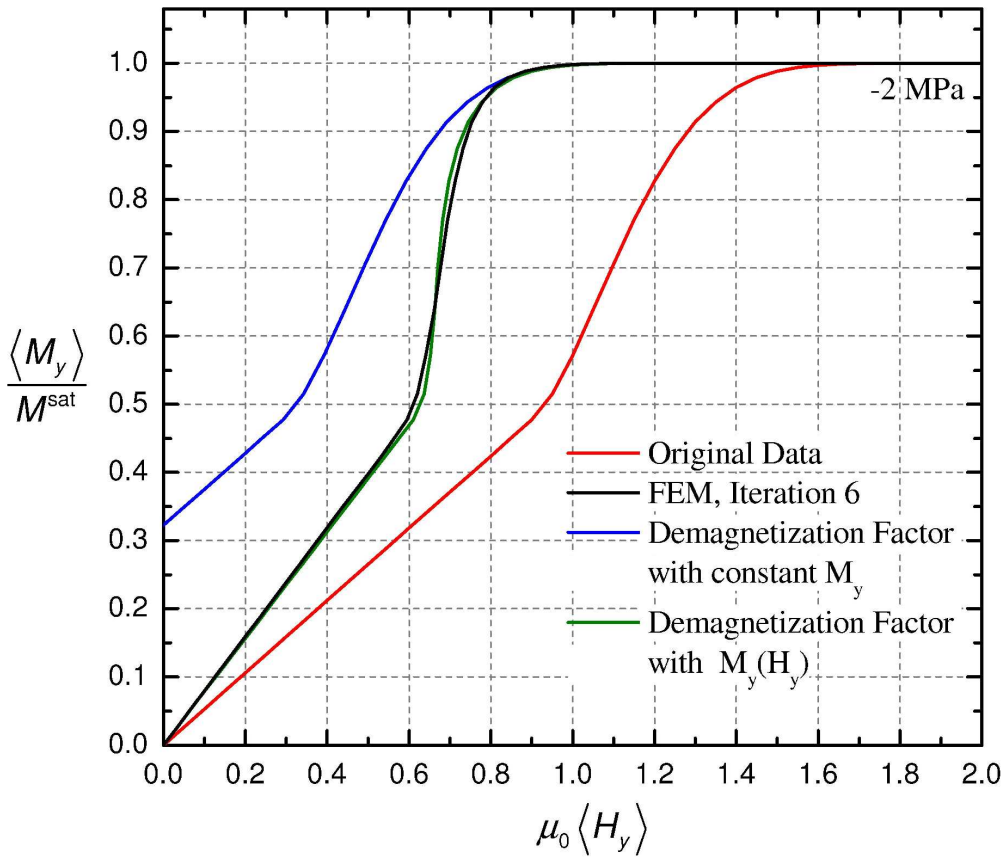

Figure 10
155x133mm (600 x 600 DPI)

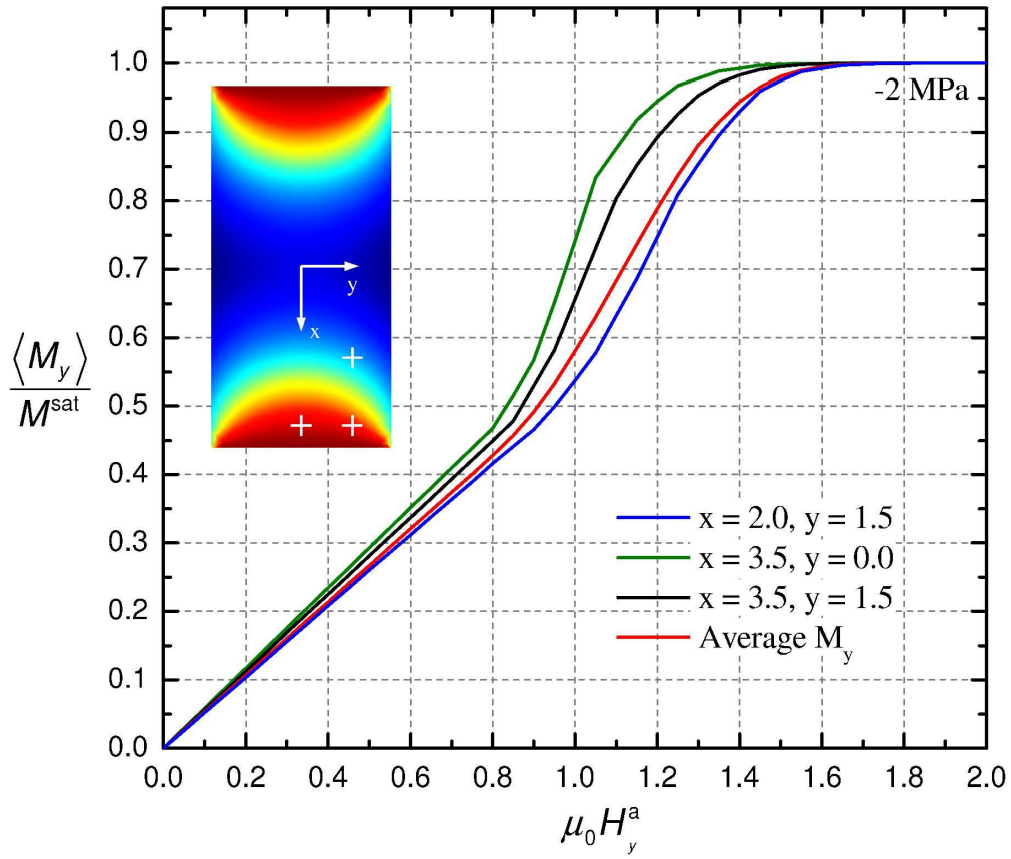

Figure 11
153x130mm (600 x 600 DPI)

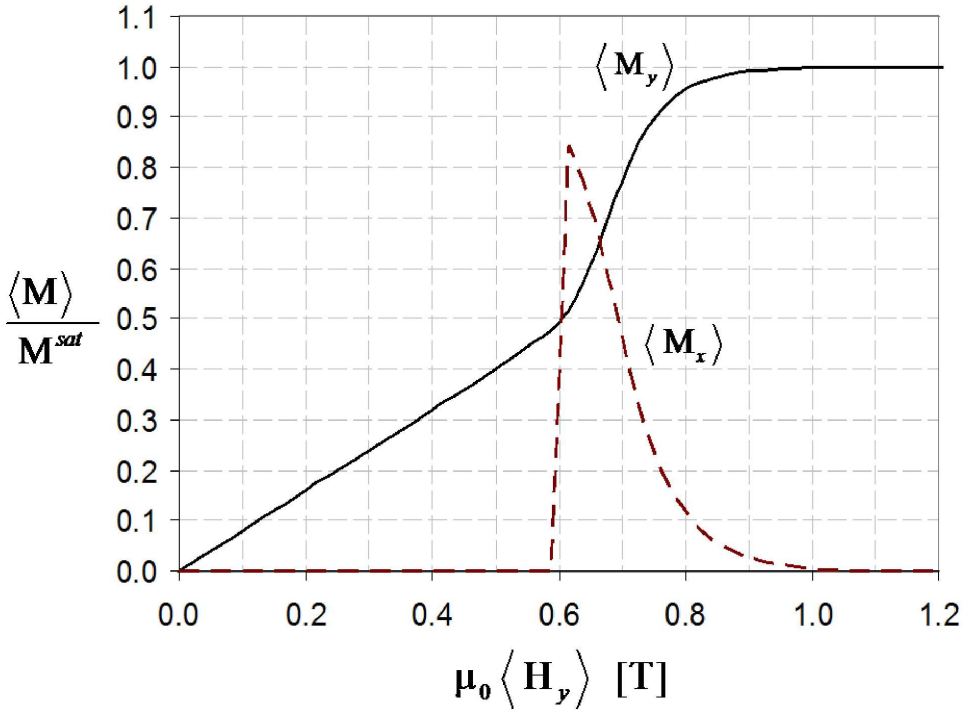

Figure 12
254x190mm (600 x 600 DPI)

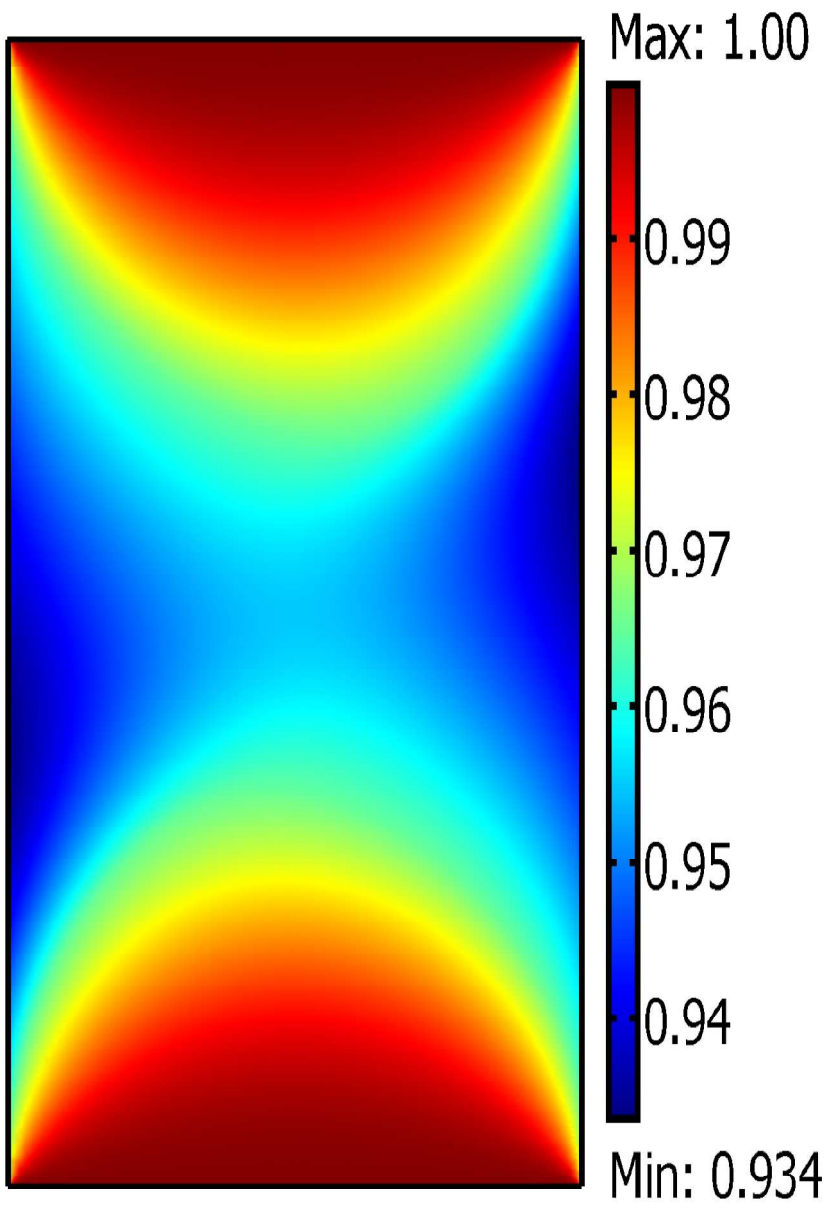

Figure 13(a)
428x614mm (600 x 600 DPI)

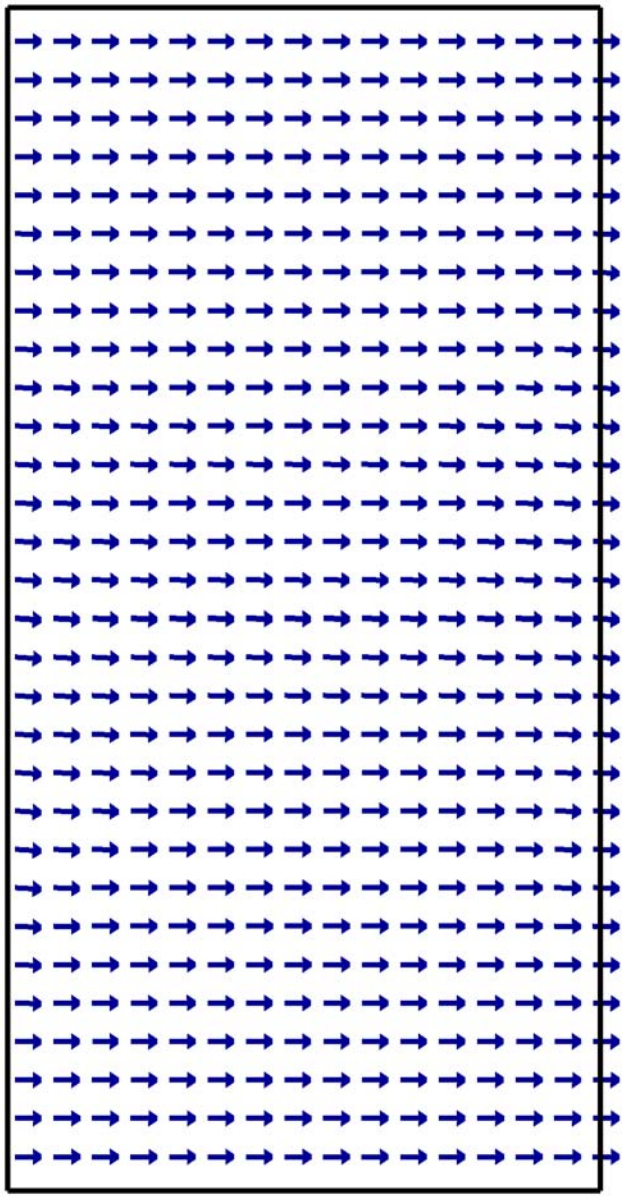

Figure 13(b)
333x640mm (600 x 600 DPI)

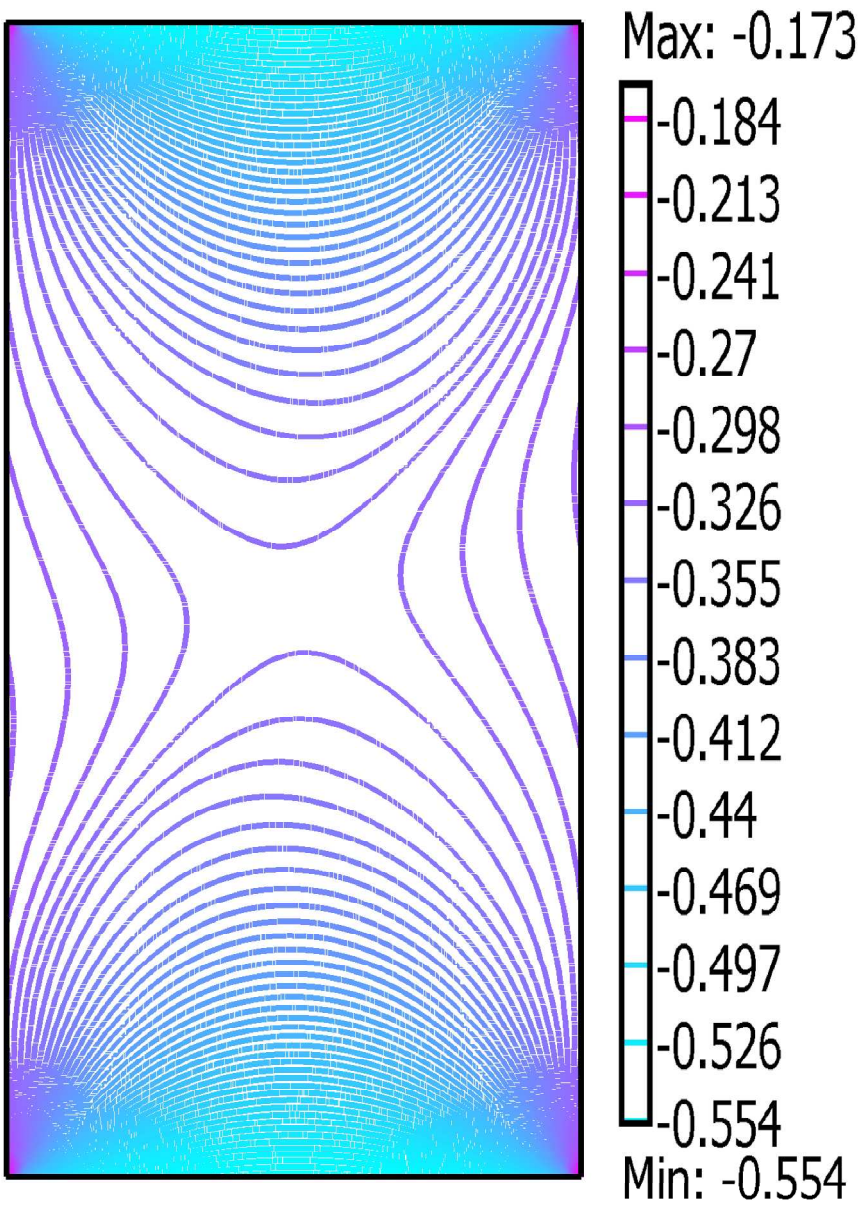

Figure 14(a)
431x600mm (600 x 600 DPI)

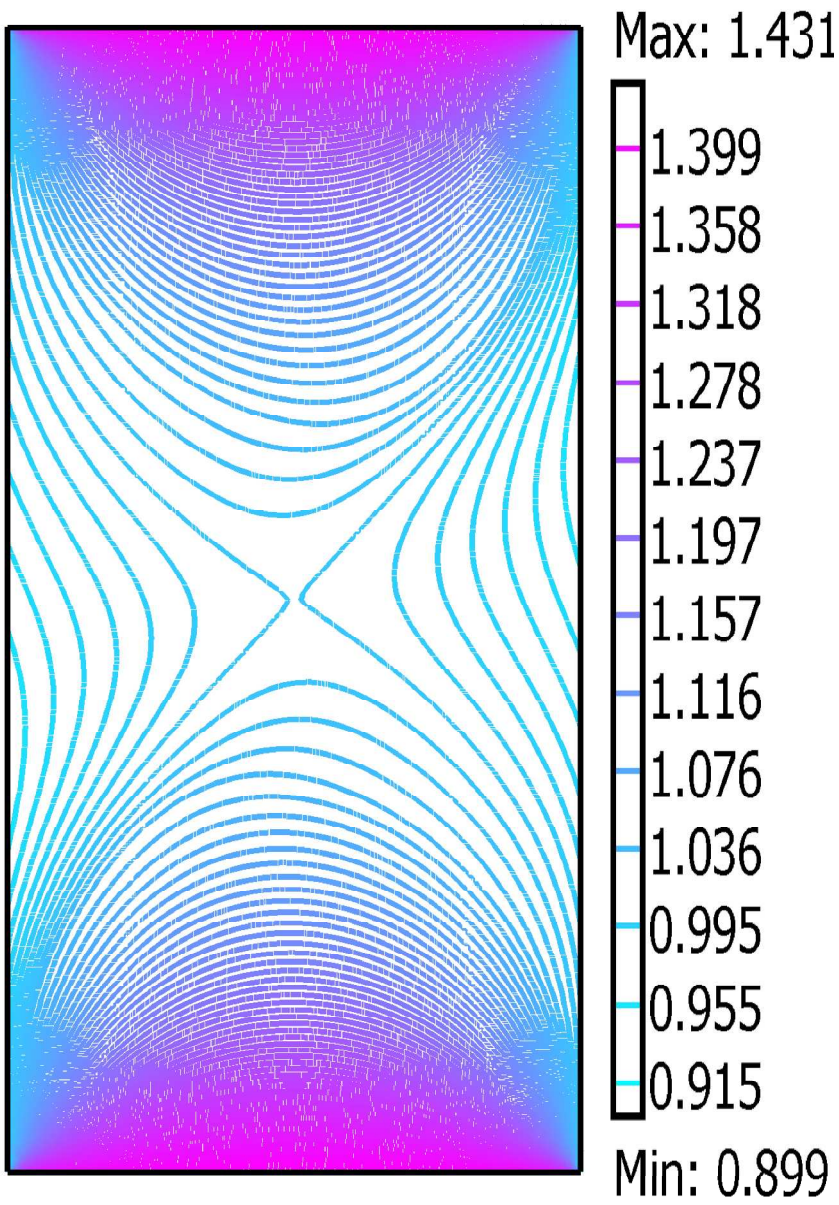

Figure 14(b)
425x609mm (600 x 600 DPI)

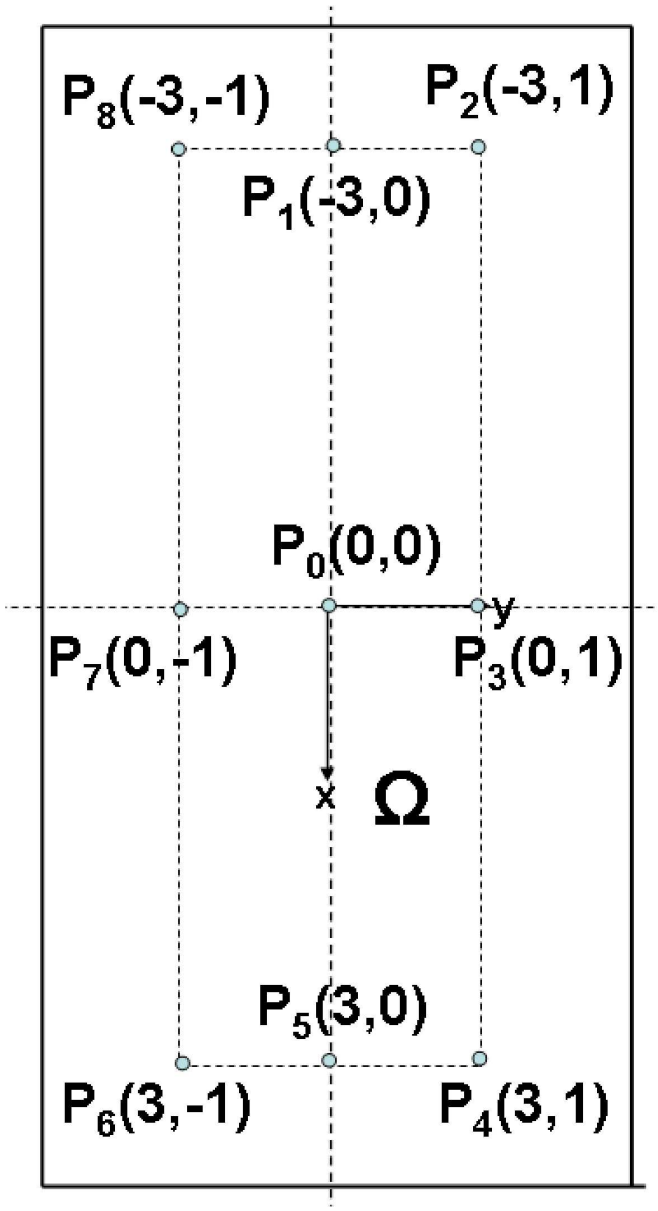

Figure 15
99x182mm (600 x 600 DPI)

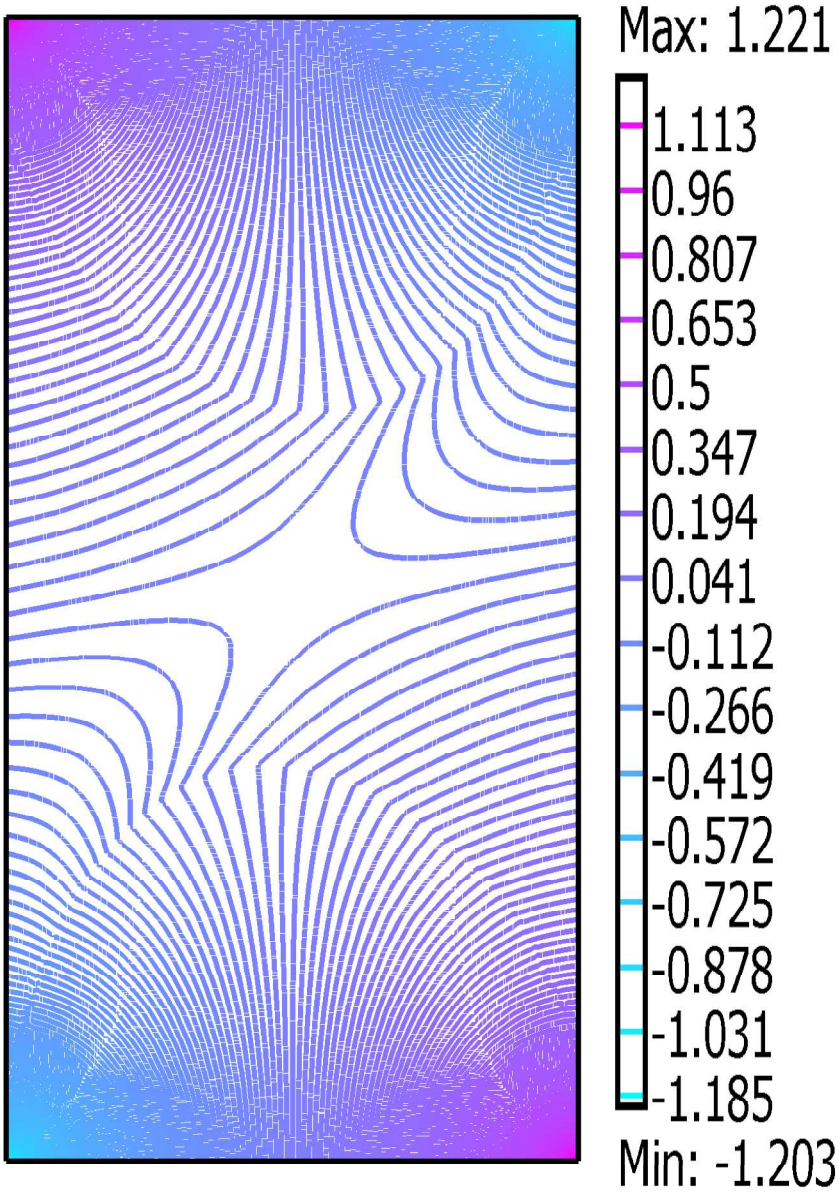

Figure 16(a)
456x644mm (600 x 600 DPI)

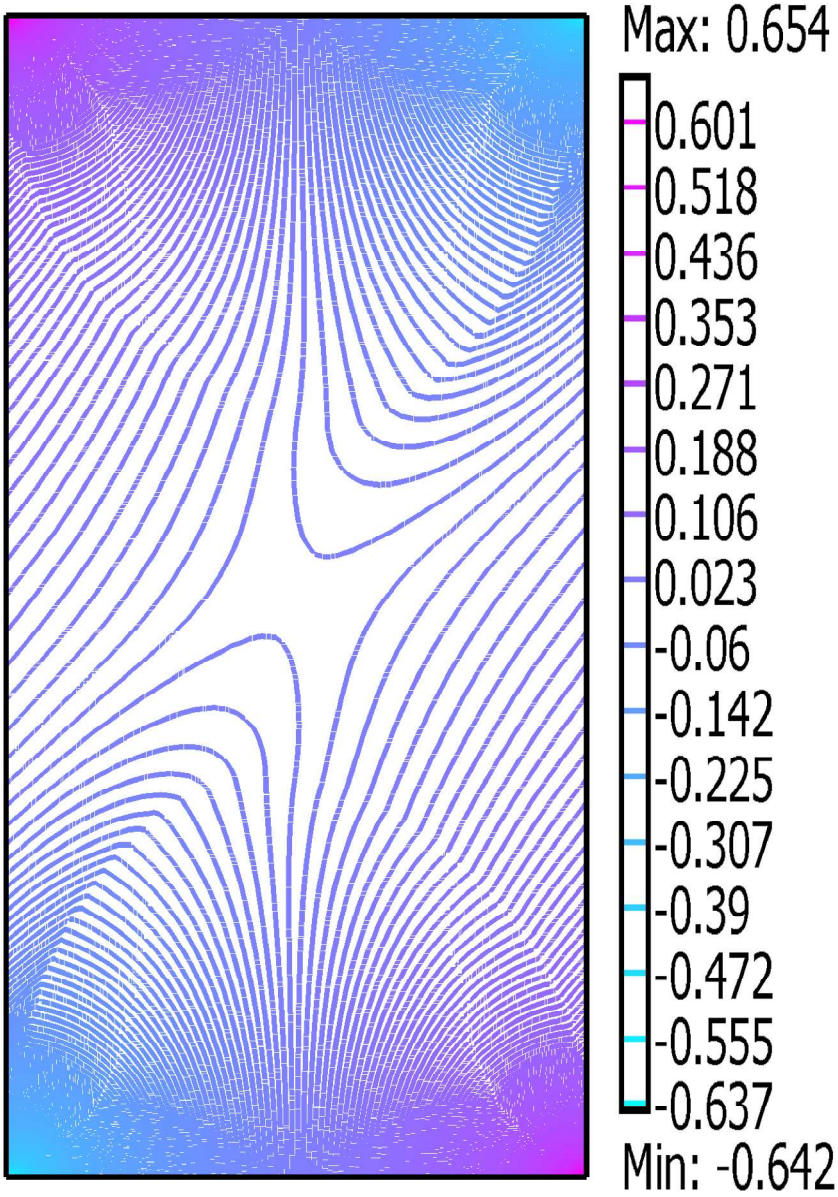

Figure 16(b)
449x635mm (600 x 600 DPI)

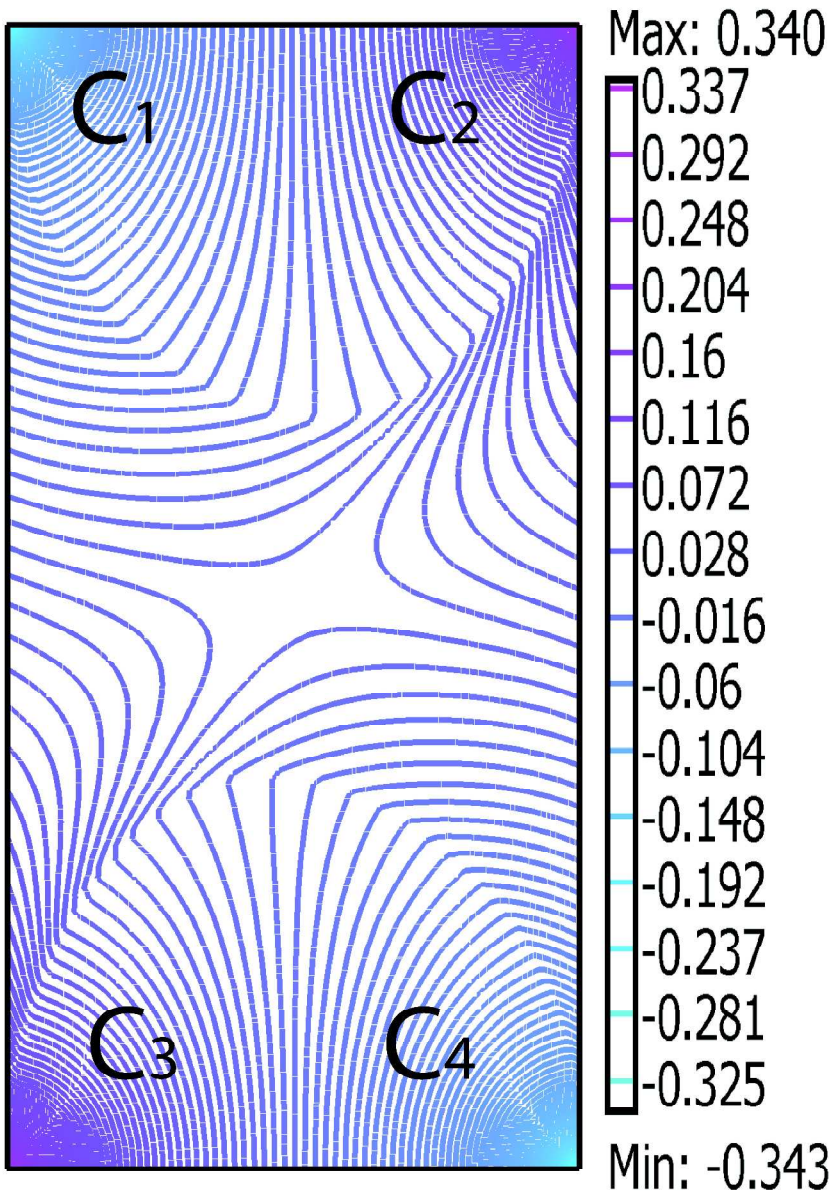

Figure 17(a)
416x599mm (600 x 600 DPI)

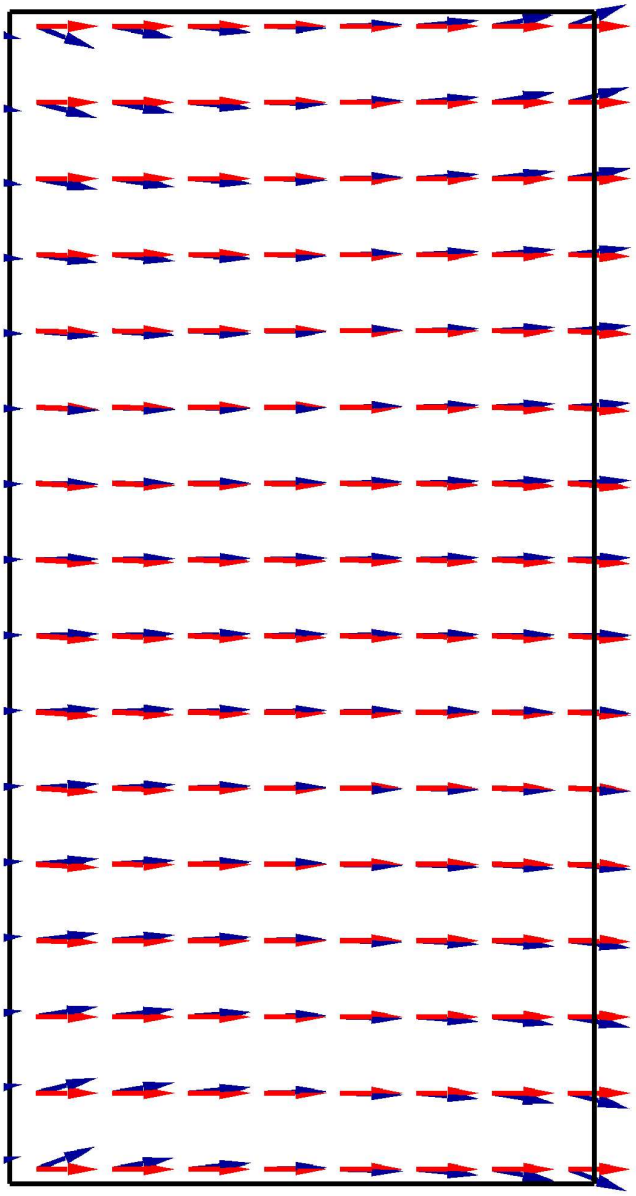

Figure 17(b)
360x669mm (600 x 600 DPI)

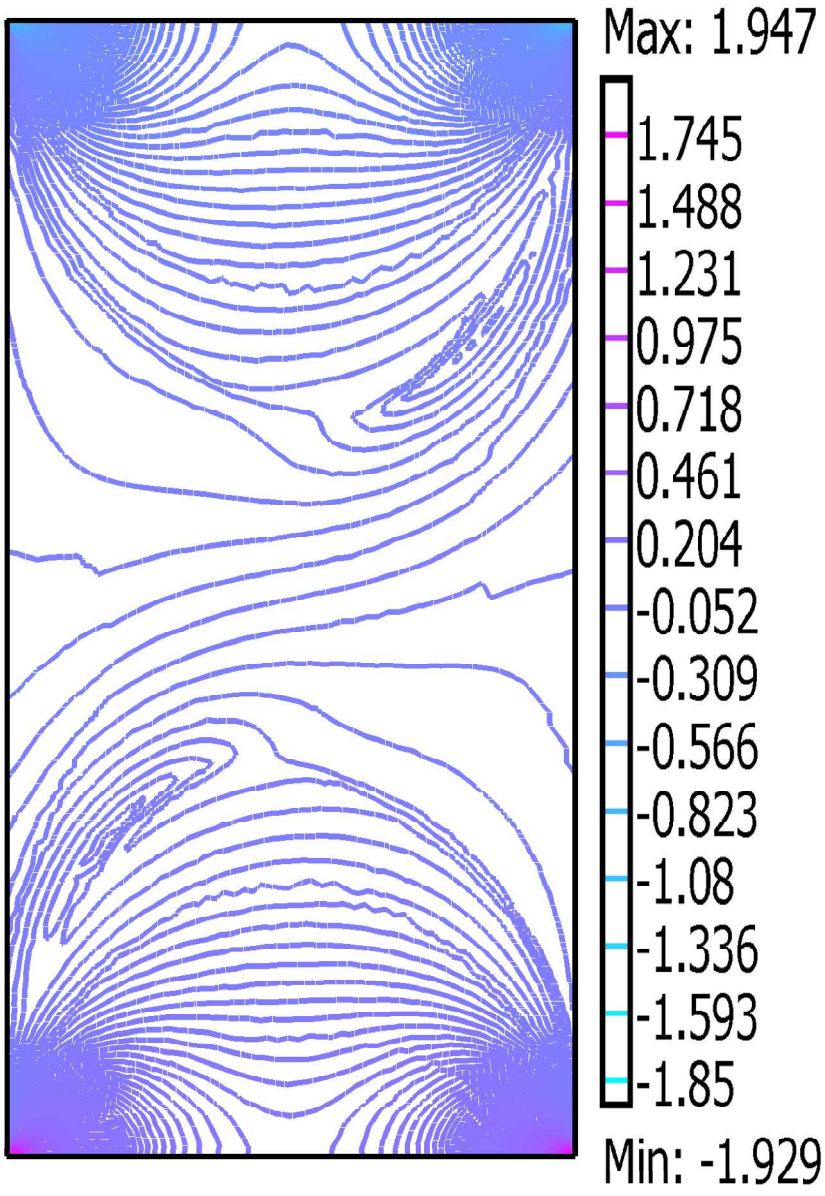

Figure 18(a)
434x628mm (600 x 600 DPI)

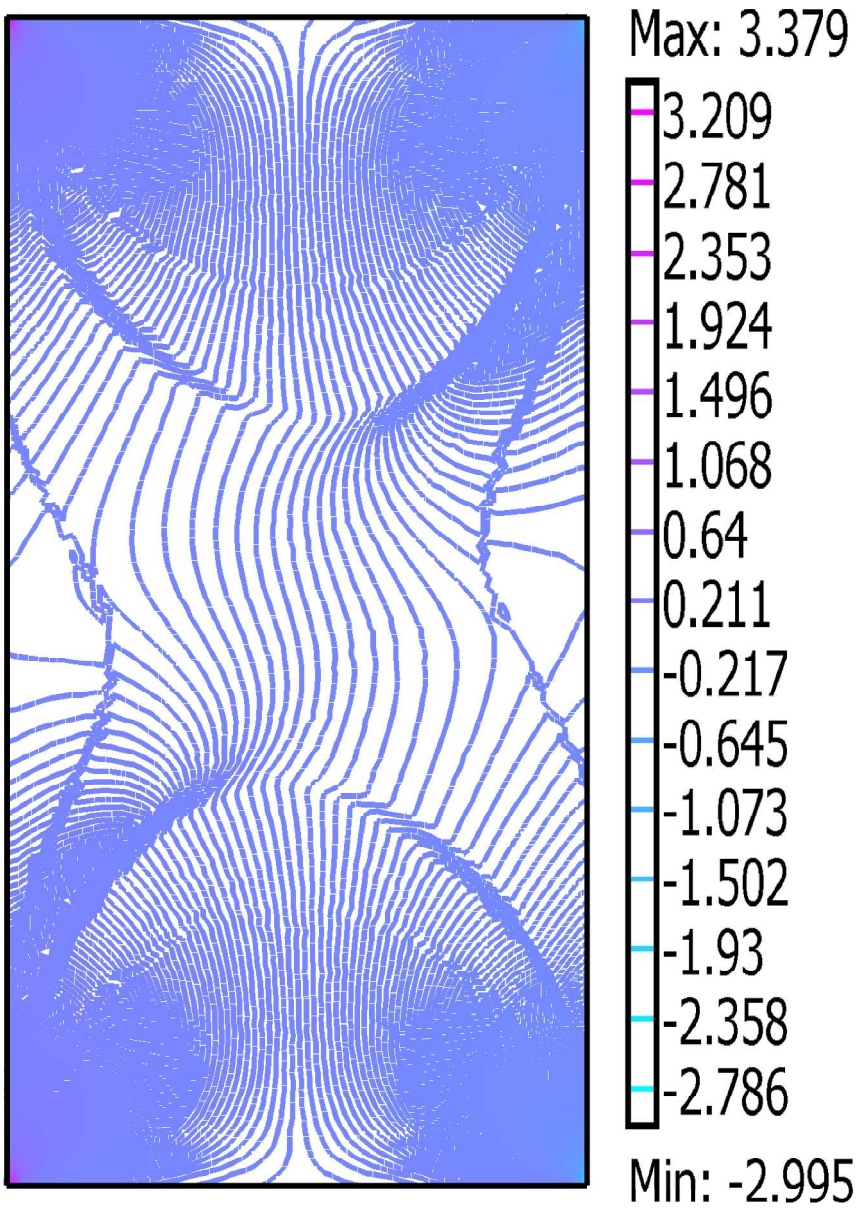

Figure 18(b)
446x614mm (600 x 600 DPI)

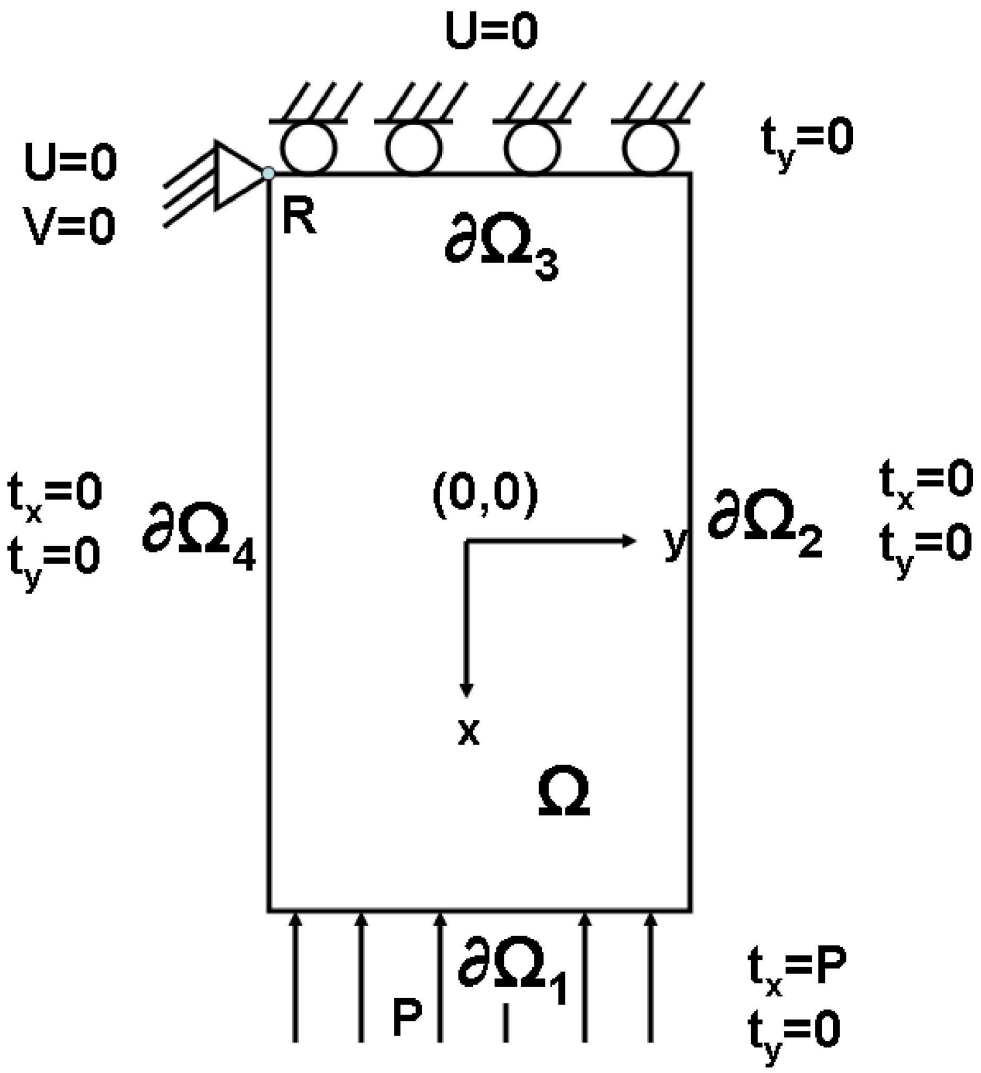

Figure 19
161x174mm (600 x 600 DPI)

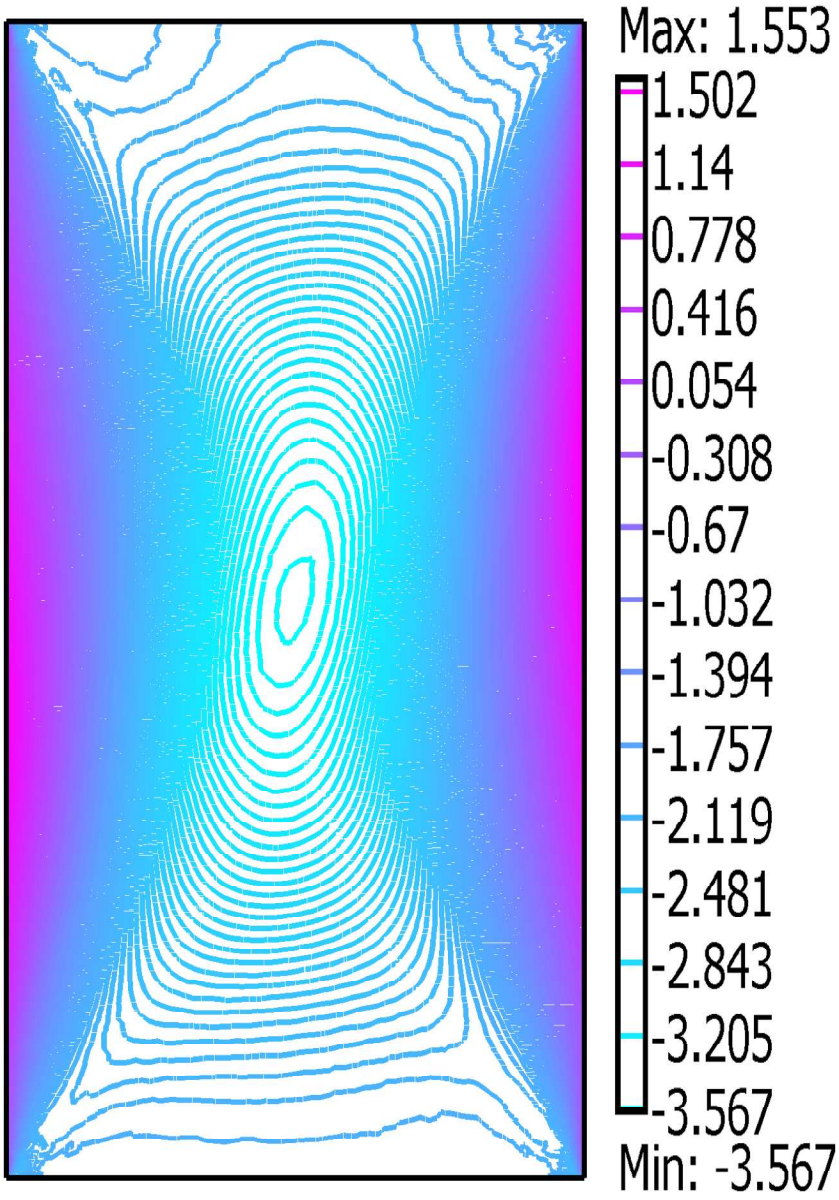

Figure 20(a)
452x640mm (600 x 600 DPI)

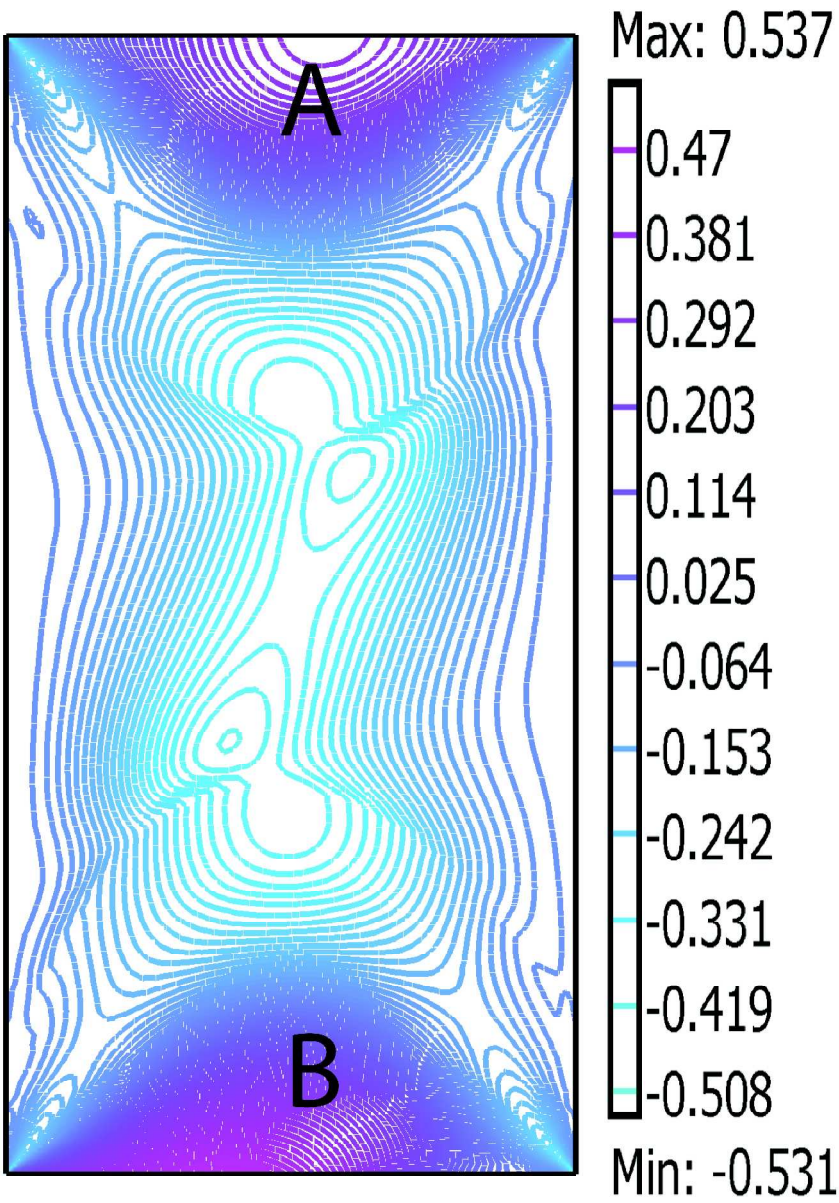

Figure 20(b)
418x589mm (600 x 600 DPI)

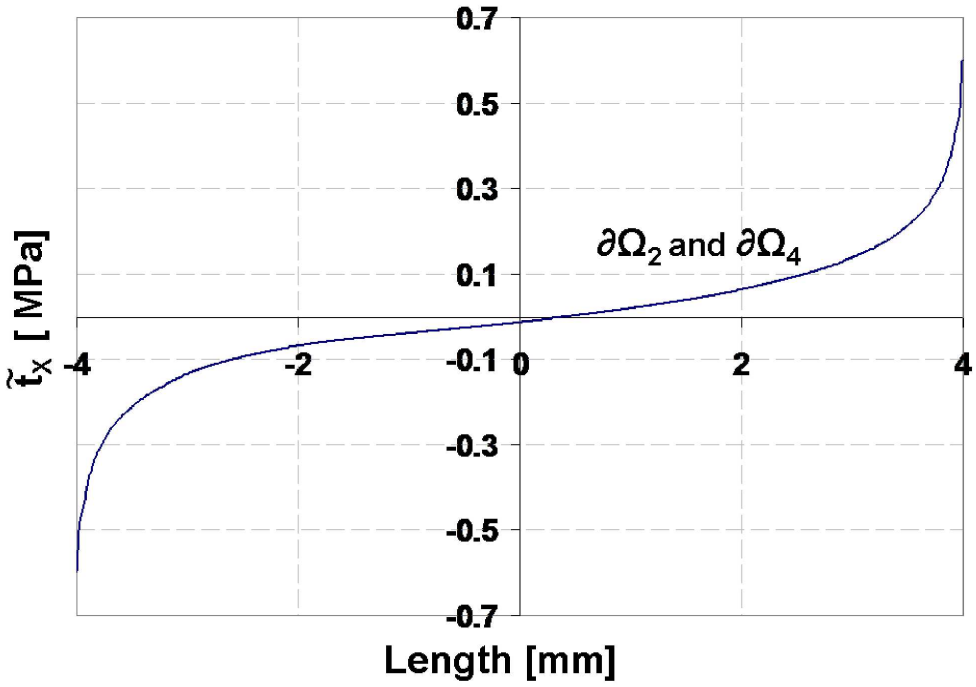

Figure 21(a)
254x190mm (600 x 600 DPI)

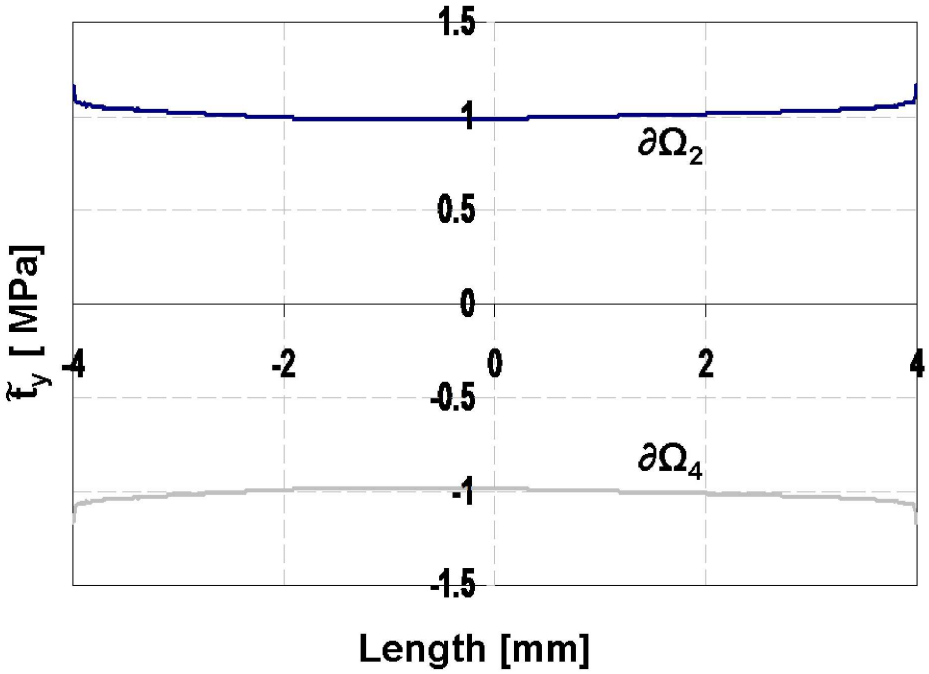

Figure 21(b)
254x190mm (600 x 600 DPI)